The Adventures of Nikita and Casper

High Power Ultraviolet Lasers for Precision Spectroscopy

by

Emily Elizabeth Altiere

B.A. (Hons) Physics, Bryn Mawr College, 2010

A THESIS SUBMITTED IN PARTIAL FULFILLMENT
OF THE REQUIREMENTS FOR THE DEGREE OF

Master of Science

in

THE FACULTY OF GRADUATE AND POSTDOCTORAL STUDIES
(Physics)

The University of British Columbia
(Vancouver)

November 2014

Abstract

The optically pumped semiconductor laser (OPSL) offers several advantages as a laser source for precision spectroscopy. The semiconductor gain bandwidth allows an OPSL to run continuous wave (CW) between 920 - 1154 nm and with a free running linewidth 500 kHz. High powers have been observed in OPSL, as high as 70 W. Paired with doubling crystals the wavelength range can be extended down to the ultraviolet (UV) with high power. This research presents an OPSL operating at 972 nm at 1.7 W sequentially doubled down twice to a wavelength of 243 nm at 150 mW. The linewidth is reduced by locking one OPSL to a Fabry-Poret stabilization cavity and then the relative linewidth was measured between two OPSL's locked together. The linewidth is determined to be 87 kHz, dominated mostly by technical noise. This laser is set to be used for cryogenic hydrogen spectroscopy and precision measurements of the Lamor precessional frequency of ^{129}Xe when it is used as a comagnetometer for measuring the electrical dipole moment (EDM) of the neutron.

Preface

Chapter 2 is based on the work of Dr. Yushi Kaneda at the University of Arizona. He is responsible for the construction of the OPSL source and the original design of the second harmonic generation (SHG) cavities. Arthur Mills and I worked together to produce the UV light through the SHG cavities, as presented in Chapter 3. The power conversion through SHG measurements in Chapter 3 were performed by myself and the linewidth measurements were performed by myself and Marc Lejay.

Table of Contents

List of Tables

List of Figures

Glossary

AC	alternating current
BBO	bicarbonate barium octate
CW	continuous wave
DBR	distributed Bragg reflector
DC	direct current
EDM	electrical dipole moment
FSR	free spectral range
FWHM	full width at half maximum
GPE	geometric phase effect
IR	infrared
LBO	litium barium octate
LO	local oscillator
OPSL	optically pumped semiconductor laser
PDH	Pound Drever Hall
PZT	piezoelectric transducer
RF	radio frequency
ROC	radius of curvature
SHG	second harmonic generation
TEC	thermoelectric cooling
UCN	Ultra Cold Neutron
UV	ultraviolet

Acknowledgments

I would like to use a few words to express my gratitude to those who helped me over the past couple of years. Most important is Dr. D. Jones, my supervisor, who has given me much support and advising throughout these years. I would also like to thank Arthur Mills for his daily support in and out of the lab. He significantly helped me generate UV light for the first time. Marc Lejay for helping out so much with the linewidth measurements and always having the laser warmed up and ready every morning. Lastly, I would like to thank those who have given me abundant support throughout my life and given me the opportunities to complete this degree. This is includes my parents, grandparents, brother and cats whom have graciously given nothing but support through the good times and bad.

Chapter 1

Introduction

This chapter presents the introduction and motivation of the development of a continuous wave (CW) high powered, narrow linewidth ($<$ 1 MHz) optically pumped semiconductor laser (OPSL) for second harmonic generation (SHG). The goal is to generate high power ultraviolet (UV) light for the use in precision spectroscopy. Sections 1.1.1 and 1.1.2 discuss the current experimental projects that motivate the work presented. This laser source has the potential to impact both the hydrogen spectroscopy and Ultra Cold Neutron (UCN) experiments, which both require a two photon transition in the UV. The continual development of this type of laser at new wavelengths will also pose an impact the greater scope of atomic and laser research. Section 1.2 will then present the OPSL source as the means for generating high powered infrared (IR) light, compared to other available sources. The OPSL is then paired with two enhancement cavities to produce SHG to achieve a high efficiency harmonics down to the UV as compared to the single-pass method.

1.1 Motivation

The general motivation to this project is to perform precision spectroscopy. Spectroscopy is the study of the atomic spectra produced when matter interacts with or emits electromagnetic radiation. In other words, the process by which an atom changes energy levels by absorption or emission of a photon. Energy transitions in atoms can be probed by electromagnetic radiation, or laser light. There are two spectroscopy experiments that motivate the research presented in this thesis. The first, is precision spectroscopy of the fundamental hydrogen atom. Hydrogen was first discovered in 1766 by Henry Cavendish, who described it as "inflammable air from metals" [4]. Since then it has been a major focus for study. This atom is not only the most fundamental atom, composed of one electron and one proton, but also has a simple energy transition. This transition consists of neither hyperfine splitting or spin states and is known as the $1s$ to $2s$ transition, as shown in Fig. 1.1. The required photon wavelength (or energy) is either a single 121 nm photon or two photons at 243 nm. 248 years after the atomic discovery, the energy required for this transition is still being measured in the effort to determine even more fundamental physics, the radius of the proton [21] . Section 1.1.1 will discuss the current efforts to refining the $1s$ to $2s$ measurement.

Scientific efforts towards reducing the uncertainties on fundamental constants stretch from the radius of the proton [21] to the electrical dipole moment (EDM) of the neutron [16]. Measurements of the EDM of the neutron have been studied since the 1950's [32]. The current experimental methods for determining the neutron EDM uses ^{199}Hg, whereas the new approach will use both ^{199}Hg and and ^{129}Xe. These isotopes are used to reduce systematic uncertainties from long term drifts and inhomogeneities in the applied magnetic field from the measurement of the neutron EDM. In terms of the spectroscopy performed, the ^{129}Xe is excited from the ground state up to the $6p$ state requiring an energy of two photons at 252 nm. Unlike the hydrogen spectroscopy experiment, the goal is not to determine the exact transitional energy, but rather to simply determine how many ^{129}Xe atoms are in a one of the two ground states. The energy levels of ^{129}Xe have hyperfine splitting and two ground states, with opposite spins. A schematic of the energy levels of interest is shown in Fig. 1.3b. Further discussion of the UCN experiment and spectroscopy are described in Section 1.1.2

1.1.1 Hydrogen Spectroscopy

Currently, the $1s$ to $2s$ transition in hydrogen, shown in the Fig. 1.1.1, is known to within an uncertainty of 10^{-15} Hz as published by H*ä*nsch's group in 2013 [21]. This is the most precise measurement to date. The efforts to improve this measurement and minimize the uncertainty are ongoing. There are several ways to do so, including improving the hydrogen source and the laser used to probe the transition. Effects from Doppler broadening are minimized for a colder hydrogen source, thus increasing the accuracy of the energy measurement. Another way to improve this measurement is with the laser source. By decreasing the linewidth of the laser source and increasing the intensity will improve measurement statistics. The energy transition can be achieved with two photons at 243 nm. An increase is laser intensity will proportionally increase the transition rate. The intensity can be increased by increasing the power of the laser or decreasing the beam size. The linewidth of the laser, which can also be thought of the certainty of wavelength, will also contribute to the uncertainty in the transition measurement. The more narrow the linewidth, the more certain the wavelength is to be the expected value and thus minimizing the uncertainty in the energy transition measurements. More about the linewidth can be found in Chapter 5, where the linewidth of the OPSL is defined and measured. This OPSL system combined with the cold hydrogen efforts by Dr. Lenz Cesar at the Federal University of Rio de Janeiro, has the potential to contribute to the precision measurements of the $1s$ to $2s$ transition of hydrogen [26].

1.1.2 Ultra Cold Neutron

The primary goal of the UCN collaboration currently under construction at TRIUMF, the Canadian national laboratory for particle and nuclear physics, is to measure the EDM of the neutron. In order for an elementary particle, like a neutron, to possess an EDM there must be a violation of both parity (P) and time inversion (T) [24]. Although several theories suggest the neutron has a non-zero EDM, the predictions vary significantly over orders of magnitude [11]. Since the 1950's measurements of the neutron EDM have reduced the upper limit on the value by six orders of magnitude, reaching a

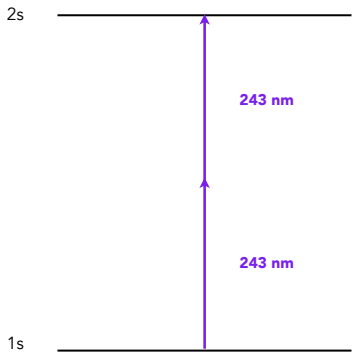

Figure 1.1: Schematic of the $1s$ to $2s$ transition of Hydrogen. This transition requires two 243 nm photons to excite.

level of 10^{-26} in 2006 [3]. One of the biggest sources of uncertainty still comes from systematic effects. To reduce these uncertainties from effects like a non-uniform field and slow drifts in the field over time, a source with a well measured EDM is used. The previous experiments by Baker *et al.* performed the experiment with Mercury, specifically ^{199}Hg [3], which has an EDM with upper bound of $|d(^{199}Hg)| < 3.1$ x $10^{-29}e$ cm [14]. The use of the additional atomic source is given the name, co-magnetometer. The use of a co-magnetometer allows the magnetic field in the system to be calibrated very accurately for a better determination of the neutron EDM by a significant reduction of the uncertainty in the magnetic field. A complete description of this experiment using ^{199}Hg can be found in the 2013 publication by Baker *et al.* [3].

The new project proposed by the UCN collaboration will use ^{129}Xe and ^{199}Hg as an atomic dual co-magnetometer. ^{129}Xe offers a higher vapour pressure than ^{199}Hg and a lower capture cross section, meaning more ^{129}Xe can be present in the trap while still avoiding collisions with the neutrons. Using both atomic species as a dual co-magnetometer allows a cross check of geometric phase effect (GPE), due to the opposite sign of the magnetic moments. This reduces some significant systematic errors in the EDM measurements. Conveniently, both the ^{199}Hg and ^{129}Xe require a UV laser source within 1.3 nm of each other. The same laser source can be used with wavelength adjustments that are within the tuning range of the OPSL laser.

This first experiment to be done is to precisely measure the EDM of ^{129}Xe using ^{199}Hg as a magnetometer. Then the next experiment will be to measure the EDM of the neutron using both ^{129}Xe and ^{199}Hg as a dual co-magnetometer. In either case, the general process is the same and detailed by Baker *et al.* [3], with a short description here. The ^{129}Xe and ^{199}Hg are spin polarized by spin exchange optical pumping, while the neutrons are polarized by passing them through a magnetized polarizing foil. The atoms and neutrons are then sent into the detection chamber, where a uniform magnetic and electric field are applied, $\mathbf{B}_0$ and $\mathbf{E}_0$, such that the spins are aligned antiparallel to $\mathbf{B}_0$. Since the goal of the experiment is to measure the EDM, the strength of the electric field is very

high compared to the magnetic field, where $\mathbf{B}_0$ is on the order of 1 μT. A resonant oscillating field, $\mathbf{B}_1$ is applied perpendicular to $\mathbf{B}_0$. The frequency of $\mathbf{B}_1$ is such that it is at the resonant frequency of either ^{129}Xe, ^{199}Hg or the neutrons. $\mathbf{B}_1$ is applied with a strength and time-duration such that the spin of the atoms or neutrons will undergo a $\pi/2$ phase shift and become perpendicular to $\mathbf{B}_0$. The measurements of the atomic sources and neutrons does not occur simultaneously. Rather the experiment alternates between the neutrons and atomic sources and continues for up to 26 hours [3].

The process of the $\pi/2$ phase shift that the atoms and neutrons undergo is similar. Fig. 1.2 shows how the spin of either the atoms or neutrons change from a spin-up state, $|+z>$, to shifting by $\pi/2$, to a superposition of the up and down states, $|+z>$ and $|-z>$. Fig. 1.2a is the Bloch sphere, where the quantization axis here is the z-axis. When $\mathbf{B}_1$ pulse is applied to the atomic, or neutron, source along the $x-y$ plane, the atomic spin will rotate and spiral down by $\theta = \pi/2$. The full $\theta = \pi/2$ occurs when the $\mathbf{B}_1$ pulse is at the precession resonance of the atomic source. From here the spin will continue to precess around angle ϕ, in a superposition between states $|\pm x>$ and $|\pm y>$. The atoms are left here to continue to precess, while the neutrons will undergo another $\mathbf{B}_1$ pulse to add an additional $\pi/2$ shift. The resulting spin state of the neutrons is measured directly by passing them through another foil. The remaining discussion here will only focus on the atomic sources and leave the neutron discussion to be read in Baker *et al.* [3].

It is worth writing out the wave function for the spin state after the $\pi/2$ shift following Sakurai [27]. To start, the initial spin state in the z-basis is given as,

$$|\psi>= \frac{1}{\sqrt{2}}(|+z>+|-z>). \tag{1.1}$$

The atoms experience a magnetic field in the z direction, giving a Hamiltonian

$$H = -\Big(\frac{e}{m_e c}\Big)\mathbf{S}\cdot\mathbf{B}, \tag{1.2}$$

where the magnetic moment is $e\hbar/2m_e c$ and $\mathbf{S}$ is the spin. The energy eigenvalues can then be written as,

$$E_\pm = \mp\frac{e\hbar B}{2m_e c}. \tag{1.3}$$

Writing the time dependent form of the wave function, Eq. 1.1 with energy eigenvalues, Eq. 1.3,

$$|\psi(t)>= \frac{1}{\sqrt{2}}(e^{iE_+ t}|+z>+e^{iE_- t}|-z>). \tag{1.4}$$

It is simple to factor out one of the energy components, providing an overall shift to the entire function and leaving a term with the difference in energies. This term is defined as the precession frequency [3], ω_p, where $\omega_p = |e|B/m_e c$ [27]. Now, Eq. 1.4 becomes,

$$|\psi(t)>= \frac{e^{iE_+ t}}{\sqrt{2}}(|+z>+e^{i\omega_p t}|-z>). \tag{1.5}$$

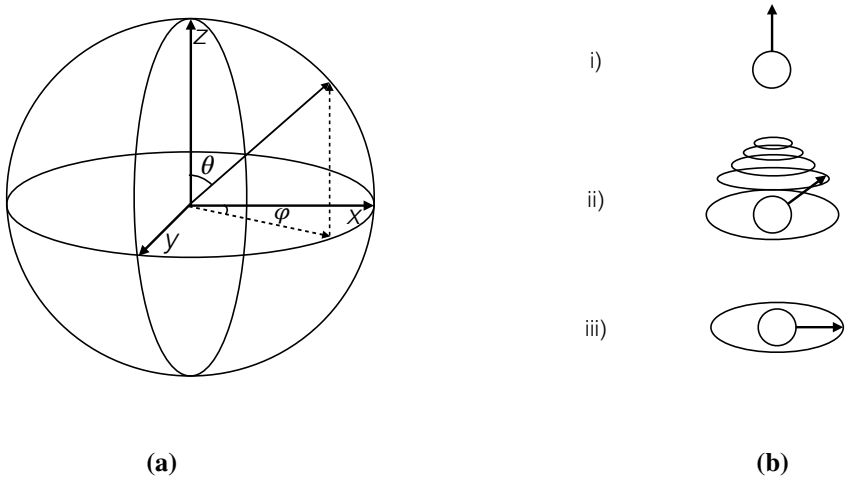

Figure 1.2: Bloch sphere and $\pi/2$ rotation of the atomic spin state. **(a)** Shows a schematic of the Bloch sphere which is a representation of the axis and angles of possible quantum spin states, $|\pm z>$, $|\pm x>$ and $|\pm y>$, and every superposition in between. **(b)** The representation of the rotation of the spin state, from spin up in (i) to a $\pi/2$ rotation in (ii) to (iii) using a pulsed magnetic field at the precession frequency of the particle.

After the atoms have gone through a $\pi/2$ shift, they are rotating in the $x-y$ plane. Thus, Eq. 1.5 can be written in the x-basis, where $|\pm z>=(|+x>\pm|-x>)/\sqrt{2}$. Eq. 1.5 becomes,

$$|\psi(t)>=\frac{1}{2}\left[(1+e^{i\omega_p t})|+x>+(1-e^{i\omega_p t})|-x>\right] \tag{1.6}$$

and simples further to,

$$|\psi(t)>=\cos\left(\frac{\omega_p}{2}t\right)|+x>-i\sin\left(\frac{\omega_p}{2}t\right)|-x>. \tag{1.7}$$

At this point, a UV laser is used to probe the atoms along the x-axis to measure their precession frequency. Both ^{129}Xe and ^{199}Hg have two ground states, as shown in Fig. 1.3. As the atoms are spinning, they will interact with the laser light as when they appear to be in the -1/2 spin state and will get excited to a higher energy state. At a rotation of π later the atoms will appear in the +1/2 spin state relative to the photons, and therefore the photons are invisible. This is the same as applying a projection operator, $\hat{P}=|-x><-x|$, to Eq. 1.7 and taking the expectation value,

$$|<\psi(t)|\hat{P}|\psi(t)>|^2=\sin^2\left(\frac{\omega_p}{2}t\right). \tag{1.8}$$

Only the sine term remains, oscillating at the precession frequency, ω_p between 0 and 1. The $|+x>$ state is known as the dark state because there is no available transition for the atoms to be excited into by the available photons. In both Fig. 1.3a and 1.3b the atoms from -1/2 state will absorb the photons, and in the 1/2 state, or when the atoms have precessed by $\phi=\pi$ rotation, they are in a

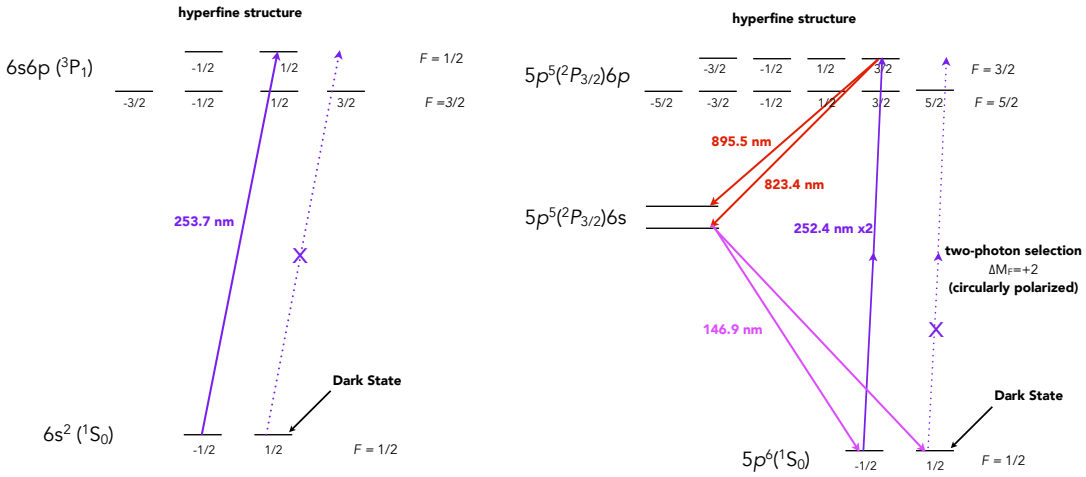

Figure 1.3: (a) ^{199}Hg transition scheme and **(b)** ^{129}Xe transition scheme used as the co-magnetometer in the UCN experiment.

dark state and absorb nothing. From this absorption, the precession frequency is measured. For the case of the ^{129}Xe, the excited atoms decay down in two steps, where in the first step they emit an IR photon, which is then easily detected to determine the precession frequency. Any changes in the magnetic field will also cause changes in the precession frequency. By monitoring the precession frequency of the atoms, ^{129}Xe and ^{199}Hg, these small field changes can be detected. The measured fluctuations and drifts in the field are then applied to the neutron measurements to remove the systematic errors. Thus reducing the uncertainty from previous measurements of the neutron EDM.

Similar to the hydrogen experiment, the energy transition for ^{129}Xe is a two photon transition. The higher power in the UV, gives a higher intensity which leads to a higher interaction rate. Different from the hydrogen experiment, the linewidth is not as crucial. The linewidth just needs to be narrow enough to ensure the correct transition is made. The next closest transition for the ^{129}Xe is 2 GHz away, so as long as the linewidth is less than 2 GHz, the laser is sufficient.

1.2 Ultraviolet Laser

Described by both Sections 1.1.1 and 1.1.2 a high powered, meaning $>$ 100 mW, CW UV laser with a narrow linewidth, $<$1 MHz is required. There are no commercially available UV laser sources, so the light must be generated in some way by laser sources at a different wavelength. One option would be to use nonlinear optics and start with a visible, 486 nm or 505 nm laser, and double the wavelength down (the frequency up) to the UV. However, this is also not commercially available. IR lasers are commercially available and can be frequency doubled twice down to the UV part of the spectrum. Toptica© has developed such a laser that includes the two SHG stages, converting IR to UV light. The ratings for this laser system, however, are specified at a UV power of $<$ 100mW and

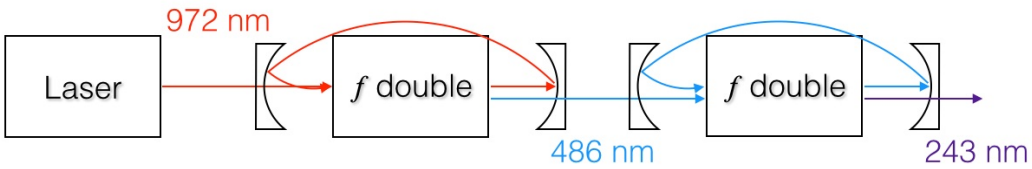

Figure 1.4: Block diagram to show the IR laser and two enhancement cavities that produce SHG at each stage. The laser source is 972 nm and frequency doubled to 486 nm at the first enhancement cavity. Then the light is frequency doubled again to 243 nm using a second enhancement cavity.

only a guaranteed linewidth of < 1 MHz.

There is a new type of IR laser available, called an optically pumped semiconductor laser (OPSL). This laser has only been available since the turn of the century. A more complete description of the laser is detailed in Section 2.1. This laser can produce high CW powers in the IR, up to 3 W, and has the potential to produce a narrow linewidth, < 1 kHz, beam. To convert the IR into UV light, there needs to be two stages of SHG.

In this experiment it is important to get the highest efficiency for the SHG. If the efficiency of the single pass is only $\sim 10^{-4}$ W^{-1} [8], then two stages would produce an overall efficiency of $\sim 0.01\%$ efficiency. The single pass efficiency varies widely depending on the crystal and the input power, as the conversion efficiency has a nonlinear relationship to the optical intensity inside the doubling element. It is clear, that single pass will not provide the desired power for these precision spectroscopy experiments. The future for this OPSL system is to provide > 100 mW of UV light. For single-pass, that would require an IR laser of 1,000 W. By placing the nonlinear crystals in an enhancement cavity the light can build up and provide higher input power into the crystal. Since the power through the crystal is 50-60 times greater than the original laser power, and efficiency of the crystals increases quadratically with increased input power, the overall efficiency is much higher. A block diagram in Fig. 1.4 shows the laser and two stages of SHG in two enhancement cavity. The total efficiency achieved in this experiment from IR to UV was $\sim 11\%$. These experimental results are shown in Section 4.2, where 1.4 W of 972 nm is converted to 150 mW of 243 nm. Thus, the UV required for the precision spectroscopy experiments of hydrogen and xenon is able to reach sufficient power.

This OPSL combined with two stages of nonlinear optics inside enhancement cavities to produce SHG has proved to produce > 100 mW in the UV. Chapter 2 will outline the experimental setup involving the OPSL and SHG enhancement cavities to produce 150 mW of 243 nm light.

Chapter 2

Experimental Method

This chapter will examine the entire experimental setup used to generate UV light from the IR OPSL. A schematic of the setup can be seen in Fig. 2.1. Each section of this chapter will focus on one part of the experimental setup. Starting with the laser source in Section 2.1, where a brief description of the OPSL technology is described that makes this laser different from all other laser sources. An overview of the enhancement cavities where the SHG takes place is outlined in Section 2.2. Finally, the optical components and the locking system used to lock each cavity to the laser frequency are presented in Section 2.3.

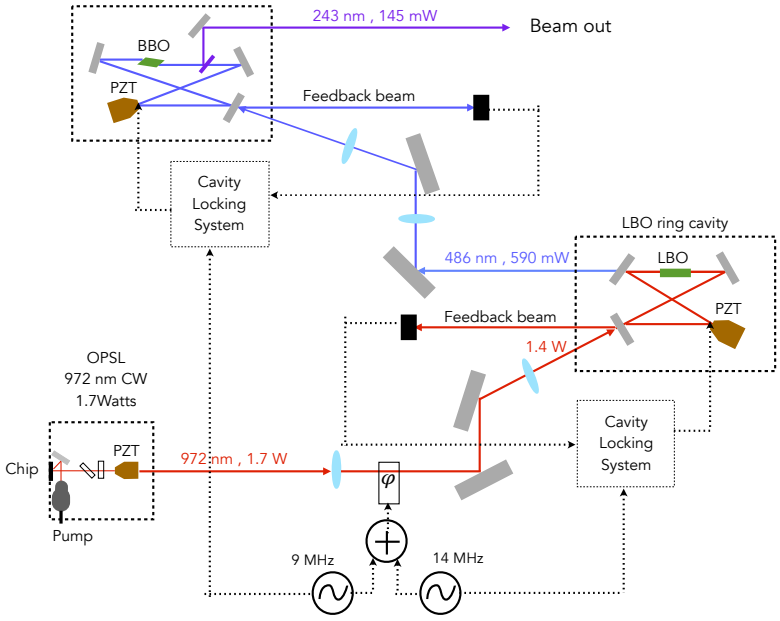

Figure 2.1: Schematic of experimental setup, including the OPSL, two doubling enhancement cavities and locking systems.

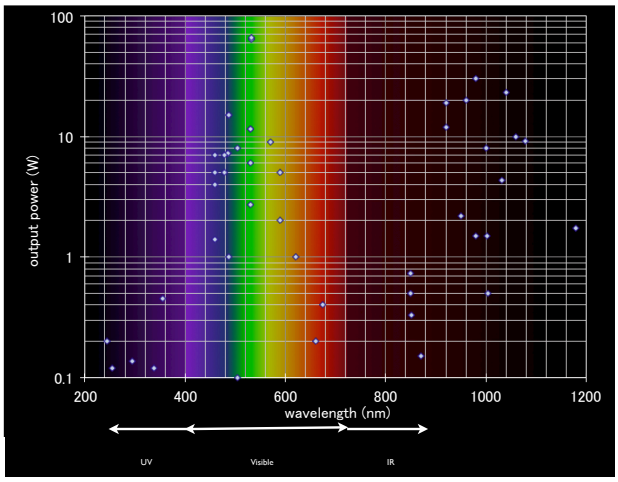

Figure 2.2: Plot to show all of the currently developed OPSLs at their various wavelengths and powers. Reproduced with permission from Dr. Yushi Kaneda [18].

2.1 The Optically Pumped Semiconductor Laser

The first and most important part of the experimental setup is the laser itself. This type of laser is commercially available from Coherent©, where a large range of wavelengths and powers, from 920 nm to 1154 nm in the IR range are offered. There are even doubled or tripled frequencies through second and third harmonic generation in a range 355 nm to 639 nm. These ranges are not continuous and there is not an available OPSL at 972 nm and thus, neither at 486 nm. The OPSL used in this experiment was designed and built by Dr. Yushi Kaneda from the University of Arizona [18] and operates at 972 nm with a power of 1.7 W. This OPSL combined with the first stage of SHG is able to produce up to 600mW of 486 nm light with a linewidth of $\sim$ 123 kHz. The results of the power shown in Section 3.2.2 and the linewidth in Section 5.3.5.

The technology for the OPSL is new and still being developed to provide more available wavelengths and powers. This type of laser was not even a commercially available product from Coherent© until 2001. Similar to a diode laser, an OPSL uses a semiconductor as the gain medium. However, instead of using current to invert the medium, as OPSL employs an optical pump. The semiconductor chip is made up of layers of semiconductor materials, Gallium Arsenide (GaAs) and Indium Gallium Arsenide (InGaAs), as shown in Fig. 2.4b [34]. When this stack is optically pumped with a diode laser, 808 nm, the photons released are in the range of 972 nm. The wavelength of an OPSL is determined by the quantum wells of the semiconductor materials of the chip. As more semiconductor materials are developed, the range of wavelengths will also increase. A table of the OPSL's that have been produced in the lab are shown in Fig. 2.2, where each point represents an OPSL with its given power. The OPSL in this experiment is not yet added to this plot, but would add a few new points, in particular one at 243 nm with 150 mW.

The power the chip is able to produce is controlled by the pumping power [34]. A higher

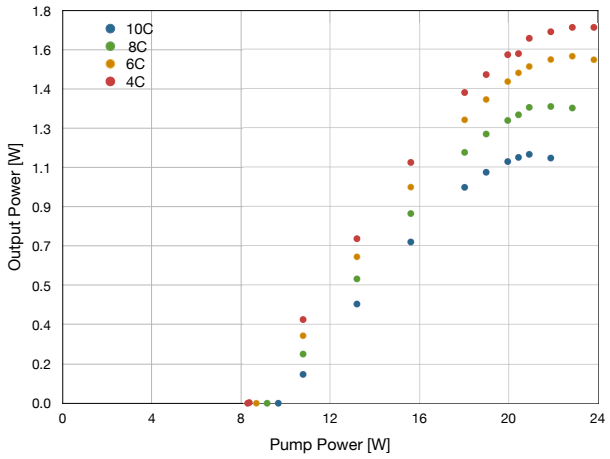

Figure 2.3: Plot of the optical pumping power to the output power of the 972 nm OPSL at four operating temperatures of the semiconductor chip. Reproduced with author's permission [18].

pumping power will increase the power in the laser, until the pumping power reaches a threshold. This is when the pump is too high, which heats up the chip, the power quickly drops off. The chip can also be cooled with water and thermoelectric cooling (TEC), or also known as a Peltier. Fig. 2.3 shows how decreasing the temperature of the chip, increases the laser power for an also increasing pump power. Once again, the point where the laser stops lasing can be seen in Fig. 2.3, when the power drops off for high pumping powers above 20 W. It is also impossible to continuously cool the chip further down, because the risk of condensation and ice arises.

Each time a new OPSL chip is grown, the chip will emit a range of wavelengths with a power dependent on the wavelength. An example of this can be seen by Wang *et al.* [34]. Here the authors also varying the OPSL chip temperatures to show how the range of wavelengths emitted shifts with temperature. The central wavelength will have the most power available. If the desired wavelength is off from the centre wavelength, it is possible to operate the OPSL here, knowing that the possible power will be compromised. To choose the wavelength of the OPSL from within the range emitted by the chip at a given chip temperature, there are two filters placed inside the laser cavity. The first is the birefringent filter placed at Brewster's angle and the second is the etalon. These filters are used in tandem to select a single longitudinal mode. A laser without filters will lase over a range of longitudinal modes, which depends on the net gain bandwidth of the laser. These modes are all separated by the free spectral range (FSR) of the laser cavity, where FSR is the speed of light divided by the length of the laser cavity. For a typical semiconductor/diode laser, the two cavity mirrors are directly attached to either end of the semiconductor chip. This gives a typical cavity length of 100 μm, yielding a FSR of 420 GHz [30]. Usually, as is the case with this experiment, a single mode laser is desired. The etalon is the most narrow filter and selects one longitudinal mode per transmission peak of the etalon. However, there are many transmission peaks of the etalon, which

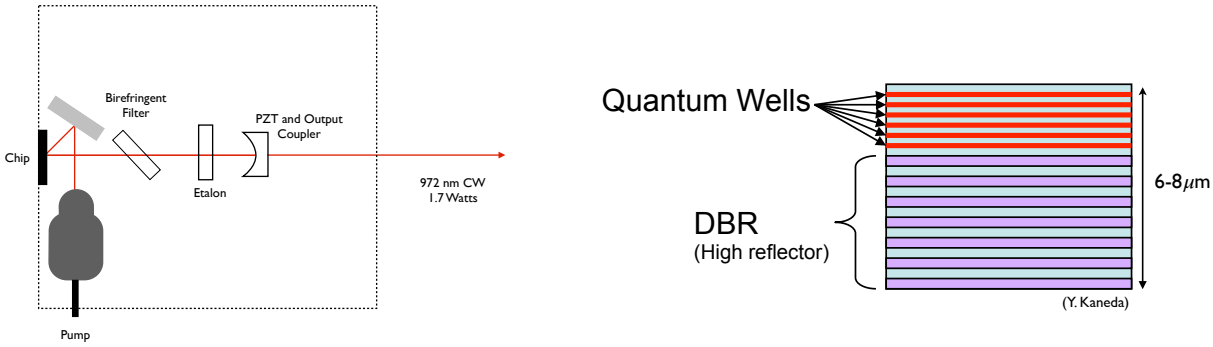

(a) **(b)**

Figure 2.4: Schematic of the OPSL head and close up of the semiconductor chip. **(a)** Schematic of the OPSL head. The pump is a diode laser, that optically pumps the semiconductor chip, or the gain medium. The birefringent filter at Brewster's angle and the etalon are filters to select the wavelength of the output and the longitudinal mode. The curved mirror is the output coupler with an attached PZT to control the length of the cavity. This OPSL provides 1.7W of CW light at 972 nm. **(b)** Schematic of the OPSL chip. It is pumped with the diode laser and emits photons in the IR. The quantum wells are the layers of Gallium Arsenide (GaAs) and Indium Gallium Arsenide (InGaAs) and the high reflector material is labeled as DBR and acts as a cavity mirror. This schematic was provided by Dr. Kaneda [18].

can still result in the laser running multi mode. The addition of the birefringent filter, which has a broader transition peak compared to the etalon and more narrow than the laser cavity, allows only one longitudinal mode to emit. By inserting the birefringent filter and etalon inside the laser cavity, and tuning the transmission peaks such that they are all aligned, it is possible to select just one longitudinal mode and run the laser single mode [30]. Both the etalon and birefringent filter are temperature controlled to fine tune the longitudinal mode or wavelength of the laser, by shifting the alignment of the transmission peaks. A close up schematic of the OPSL can be seen in Fig. 2.4a with all of the above mentioned components in their relative positions. It can also been seen that the OPSL cavity is a simple two mirror standing wave cavity. The obvious mirror is the curved output coupler, where the second mirror is a highly reflective material, called distributed Bragg reflector (DBR), under the stacked semiconductor materials of the gain medium. The overall structure of the laser is simple and similar to some other lasers, like the Ti:Sapphire laser, but the technology of the OPSL chip is the unique component that gives the OPSL a big future in changing laser technology.

The OPSL used in this experiment produces 1.7 W of power at 972 nm. The limit of this power is due to the semiconductor chip. The desired wavelength of 972 nm is not at the peak of the spectrum produced by the chip, so the maximum power possible is reduced. From Fig. 2.1 the light from the laser is sent into an optical enhancement cavity where the light undergoes SHG. The experimental

setup of these is described in the next section.

2.2 Frequency Doubling Enhancement Cavities

The motivation to develop this laser system is to provide UV light for precision spectroscopy. The OPSL is an IR laser at 972 nm. Through the use of nonlinear optics the laser light is converted down to the desired UV light at 243 nm. The process of transforming a fundamental beam into a beam with half the wavelength, or double the frequency, is called second harmonic generation, SHG.

The first observation of SHG was made by Franken, Hill, Peters, and Weinreich (FHPW) and published in 1961 [12], where they used a pulsed ruby laser with a crystalline quartz sample. Only one year later in 1962, phase-matching was discovered [13] and [20], which increased the interaction length in the crystal allowing for higher conversion efficiencies. The physics of phase-matching is described in Section 4.1. The introduction of the gas laser in 1963 was the first presentation of CW SHG [1]. Here 5 x 10^{-12} W of second harmonic for a 0.7 mW input power, for a maximum efficiency of 7 x 10^{-9}. Ashkin *et al.* were able to show that the use of CW laser allowed for easier optimization of phase-matching the crystal and well as an overall higher efficiency [1]. Only a few years later in 1966, Ashkin *et al.* presented results to highlight the stability of SHG in a resonance cavity external to the laser cavity [2]. That is, to place a nonlinear crystal in an enhancement cavity that is separate from the laser cavity.

This approach of enhancement cavities around a nonlinear crystal is the approach used in this experiment to double the frequency of the laser twice, from the IR to the UV. The experimental setup in Fig. 2.1 shows a schematic of both of the SHG laser cavities. The first enhancement cavity uses a litium barium octate (LBO) nonlinear crystal for conversation from 972 nm to 486 nm and the second cavity uses a bicarbonate barium octate (BBO) nonlinear crystal for conversion from 486 nm to 243 nm. The LBO and BBO are part of the borate crystal family, which was not developed until 1979 [8]. Previous nonlinear crystals did not extend transparency down to the deep UV (below 200 nm) or with high enough nonlinear coefficient, d_{eff}, for SHG. The significance of d_{eff} can be seen in Section 4.2, where $\gamma_{SH} \propto d_{eff}^2$ and γ_{SH} is the nonlinear conversion factor. Thus, a higher d_{eff} gives a higher SHG conversion factor.

In the hunt for funding crystals that could generate light down in the deep-UV, Chen *et al.* developed the borate compounds [8]. This compound allows for hundreds of different crystal options. The BBO was first developed, exhibiting a transparency range down to 185 nm, followed closely by the development of the LBO, with a transparency range reaching even deeper into the UV. Today, the LBO and BBO are a very commonly used pair of crystals to convert IR to the UV. The reasons for choosing the LBO for the first stage of SHG from the IR to visible is due to the phase-matching, damage threshold and SHG efficiency. The same is true for the BBO and why it is chosen to convert visible light to the UV [8]. It is from Ashkin *et al.* work from 1966 and Kozlovsky *et al.* [19] that the theory used to evaluate the SHG in the doubling cavities presented is derived in Chapter 4.

2.3 Optical and Electronic Components

The final components in the experimental setup are the optical mirrors and lenses. These components are used in between the laser and enhancement cavities. They are not simply there for aligning the beam into the cavities, but are special components for ensuring maximum efficiency in the SHG. Essentially, the beam entering into the optical cavities needs to have the same spatial TEM_{00} mode required by the cavities. To do this, lenses are placed along the beam path to focus the beam and create the desired beam size to match the desired beam size of the cavity. This process is called *mode-matching*. A more complete discussion of mode-matching is given in Section 3.2.2.

The experimental setup in Fig. 2.1 also shows the cavity locking systems. There is one for each of the two SHG cavities. The locking systems use the Pound Drever Hall (PDH) locking scheme [5] as described fully in Section 3.3. This locking system requires the fundamental laser frequency to be phase modulated. The modulation is applied through a phase modulator, run at two frequencies, which are combined through a step-up transformer. The modulator, step-up transformer and modulation frequencies are shown in the Fig. 2.1 at the bottom of the schematic and denoted by, ϕ.

The next chapters will describe the components and the theory for generating UV light from IR light through enhancement cavities and SHG. Finally Chapter 5 will separately describe the experimental setup and results for measuring the linewidth of the OPSL.

Chapter 3

Enhancement Cavities for Second Harmonic Generation

This chapter presents the theory and experimental methods for enhancement cavity resonators used for second harmonic generation, SHG. Two ring cavities, or bow tie cavities, are used in this experiment, each to enhance the power of the input beam entering the crystal and to double the frequency through SHG by means of the crystal's nonlinear susceptibility. A full discussion of the SHG from these enhancement cavities is the focus of Chapter 4. This chapter starts with the basics of enhancement cavities in Section 3.1. This includes an introduction to enhancement cavities and the concepts of FSR, finesse, and linewidth in Section 3.1.1. Following closely in Section 3.1.2, is the theory of impedance matching in order to optimize the enhancement of the light inside the cavity. Section 3.2 discusses the experimental method and results for matching the spatial mode of the input beam to the two enhancement cavities used in this experiment. Finally, the chapter concludes with a discussion of the locking scheme used to lock the enhancement cavities on resonance with the laser in Section 3.3. The locking scheme used is known as Pound-Drever-Hall, (PDH).

3.1 Enhancement Cavity Basics

An optical cavity consists of mirrors placed in a specific geometry to reflect the light between the mirrors. If the position of the mirrors are angled just right and the light is aligned to hit the mirrors at the correct position, the light will reflect around the cavity, over and over on itself. The electric field component of the the light after each round trip will add together continuously inside the cavity, enhancing the overall power of the light. These enhancement cavities are a crucial component to this experiment. The basic properties of these cavities are described throughout this section.

3.1.1 Cavity Characteristics

There are two main types of optical cavities, a Fabry-Perot and ring cavity. A schematic of both types can be compared in Fig. 3.1, where both types of cavities are used to enhance the light that

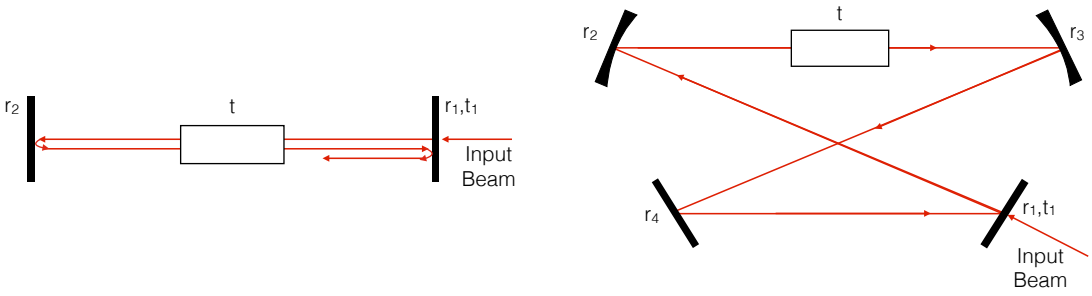

(a) **(b)**

Figure 3.1: Resonator cavity geometries. **(a)** Is a two mirror, Fabry-Perot cavity, where the light gets reflected back and forth between the two mirrors. **(b)** Is a ring cavity, where the lights gets propagated around the cavity in one direction. In both **(a)** and **(b)**, r_1 and t_1 are the reflection and transmission field coefficients of the input coupler. r_n's, where n = 2, 3, etc. are the field reflection coefficients from the other mirrors in the cavity and t is the field transmission coefficient through the optical component, i.e. nonlinear crystal.

enters into the cavity. To discuss how the light enhances inside the cavity, it is best to consider the intensity of the light. The input light enters the cavity through one of the mirrors, known as the input coupler, where some light is transmitted and some is reflected. For the cavity in Fig. 3.1a with only two mirrors, the field inside the cavity reflects back and forth between the mirrors, causing the waves to overlap. This means that the field inside the cavity is a superposition of two transverse waves that results in a standing wave. For the ring cavity in Fig. 3.1b the field inside the cavity only travels in one direction around the ring. This means that the field simply adds together in the direction of propagation.

The intensity of light, I is determined by the square of the electric field, E given by,

$$\frac{I_{r,c}}{I_0} = \left|\frac{E_{r,c}}{E_0}\right|^2 \tag{3.1}$$

where r and c are related to the reflected and circulating intensity, respectively. Both I_0 and E_0 are the intensity and field of the input beam. The reflection intensity discussion will be saved for Section 3.3, while the circulating intensity is important to define the characteristics of the enhancement cavities. The circulating intensity can also be written in terms of the optical properties of the cavity components as well as the phase of the field inside the cavity. The reflectivity's of the mirrors are given by r_1 for the input coupler and r_m for the remaining components in the cavity, where $r_m = r_{tot}t$ and r_{tot} is the product of the reflectivity's of the remaining mirrors. The term $t^2 = 1 - losses$, where the losses are from the other optical component(s) in the cavity, like a nonlinear crystal. The literature deals with the transmission and reflectivity of mirrors in different ways, but here, $r^2 + t^2 = 1$, where r and t and the electric field reflection and transmission coefficients. After one round trip

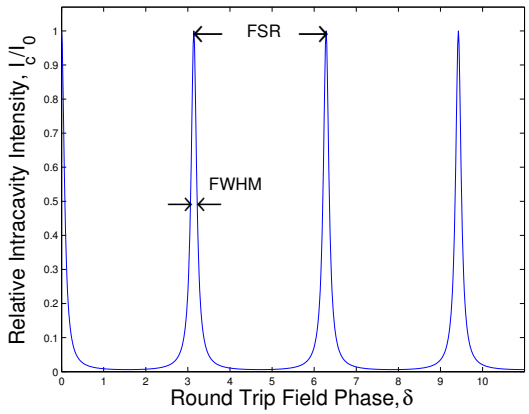

Figure 3.2: Normalized intensity profile of the circulating light inside the cavity for a varying round trip phase. The full width at half maximum, FWHM, are shown as the width of the intensity peaks and the spacing between the peaks are labeled as the free spectral range, FSR. The intensity in the cavity remains low until the round trip phase of the field is zero and the circulating intensity peaks.

the field with exhibit a phase with respect the the incoming light and denoted as, δ. The total one directional circulating intensity over the intensity of the input light is given by,

$$\frac{I_c}{I_0} = \frac{t_1^2}{(1-r_1 r_m)^2 + 4 r_1 r_m sin^2(\delta/2)}. \tag{3.2}$$

The input coupler mirror is defined separately from the rest of the cavity for several reasons. Mainly, the reflectivity of the input coupler will be lower than the other mirrors in the cavity. This is so light can enter into the cavity, as well as to satisfy the condition known as *impedance matching*. This concept of impedance matching will be further discussed in Section 3.1.2.

A visual representation of the circulating intensity of the light from 3.2 over the round trip phase is shown in Fig. 3.2. The most obvious observation is the peaks of intensity at specific values of the phase. This occurs when the cavity is on resonance, or when the phase shift is some integer number of 2π after one round trip of the light inside the cavity. When the phase is an integer multiple of 2π, there is constructive interference of the electric field components, resulting in a peak of the circulating intensity. Experimentally, the phase of the field is varied by changing the length of the cavity, using a PZT attached to one of the cavity mirrors. To experimentally see the peak in power, it is impossible to measure the power in the cavity, without disturbing the system. Rather, a little light leaks out of the cavity mirrors, as they at not 100% reflective. This light is monitored on a photodetector. The leakage will peak in power when the circulating power peaks.

The intensity profiles of the circulating light can provide valuable information about the cavity. Two cavity characteristics can be determined straight from the transmission signal. In terms of the length of the cavity, the peaks occur when a whole number of wavelengths fit inside the cavity, so the

	Finesse	Free Spectral Range	Linewidth
LBO	297	1.29 GHz	4.4 MHz
BBO	265	0.85 GHz	3.2 MHz

Table 3.1: Characterizing values of the two enhancement cavities for SHG.

periodicity is every λ for the ring cavity and every $\lambda/2$ for the Fabry-Perot cavity. When the signal from the photodetector is measured the peaks occur on a time scale, rather than phase or cavity length. The amount of time it takes the PZT to scan from one resonance to another, or the axial spacing between cavity modes, is called the free spectral range, FSR. Mathematically, $FSR = \frac{c}{L}$, where c is the speed of light and L is the length of the cavity after one round trip. In practice, FSR is reported as a frequency. The FSR of a cavity can simply to be changed by changing the length of the cavity and nothing else. In addition to the FSR, the width of the peaks also contains important information about the cavity. The FWHM of the peak is used as a metric for the linewidth of the cavity. These two cavity parameters can be seen in Fig. 3.2, for an arbitrary linewidth.

The FWHM can also be computed mathematically, by using the optical parameters of the cavity, r_1 and r_m in this case. The full relationship is given as

$$FWHM = \Delta\nu_{1/2} = \frac{2(1-r_1 r_m)}{\sqrt{r_1 r_m}} \text{ [22]}. \tag{3.3}$$

The definition of FWHM is when the amplitude of the intensity falls to half the intensity. When computing the FWHM Eq. 3.3 is used, but in practice the FWHM is quoted as a frequency. As either the reflectivity from the input coupler or other mirrors in the cavity decreases, the FWHM will become larger, meaning the width of the peaks in Fig. 3.2 will broaden.

When the ratio of the FSR and FWHM is taken, the result is also a physically significant value. This dimensionless ratio is called the finesse, $\mathcal{F}$. Finesse is widely used to describe an optical cavity, where high finesse is on the order of $10^3 - 10^4$ and low finesse cavities go down as low as $1-10$. In practice, to make a high finesse cavity, the mirrors would have very high reflectivity's of $> 99.99\%$ with a negligible amount of additional cavity losses. A low finesse cavity usually has lower mirror reflectivity's, especially the input coupler, and also would include additional components in the cavity that add loss, like a nonlinear crystal. From Fig. 3.2, a high finesse cavity would have narrow peaks that are far apart and a low finesse cavity would have wide peaks that are close together.

Similar to FWHM, finesse can also be defined mathematically by the optical parameters in the cavity,

$$\mathcal{F} = \frac{FSR}{\Delta\nu_{1/2}} = \frac{\pi\sqrt{r_1 r_m}}{1-r_1 r_m}. \tag{3.4}$$

A complete set of value for the finesse, FSR, and FWHM determined for the two cavities used in this experiment are given in Table 3.1. The reflectivity's of r_1 and r_{tot} where measured in the lab and the excess loss through the nonlinear crystals are taken to be 0.5% for the LBO and 0.3% for the BBO.

Finally, the last important quantity in an optical cavity is the enhancement, simply given as the finesse/π for the impedance matched case. This means that for a higher finesse cavity, the enhancement will be greater. It seems more desirable to have a higher finesse cavity in this case. However, because the enhancement cavities in this experiment are also creating SHG light from the fundamental, there are limits to the finesse and enhancement in order to optimize on the SHG. This will be examined further in Chapter 4.

3.1.2 Impedance Matching

In this section the concept of impedance matching will be discussed in detail. Essentially, impedance matching means that the loss through the input coupler is equal to the loss from the remaining mirror and optical component(s) in the cavity, or mathematically speaking, $r_1 = r_m$. When a cavity is perfectly impedance matched the reflection dips from the input coupler will reach zero on resonance as the phase, δ, between the electric fields in and out of the cavity is zero. The circulating power, or enhancement, inside the cavity will also be at a maximum. The representation of the circulating intensity was given in Eq. 3.2, which simplifies to,

$$\frac{I_c}{I_0} = \frac{t_1^2}{(1 - r_1 r_m)^2}, \tag{3.5}$$

when the $\delta = 0,\ 2\pi,\ 4\pi,\ etc.$ on resonance.

For a fixed loss in the cavity, r_m, and varying reflectivity of the input coupler, r_1, Eq. 3.5 produces Fig. 3.3a. Both optical cavities used in this experiment, containing the LBO and BBO crystals, have been evaluated separately. The point of highest normalized circulating to input intensity corresponds to the condition when the cavity is impedance matched. The distinct shape of the curve depends on r_m as can be seen between the LBO and BBO. The r_m value is smaller for the BBO, meaning there is more loss within this cavity. On both curves when $r_1 < r_m$ the cavity intensity gradually rises, called under-matching, and fall off very quickly for $r_1 > r_m$, over-matching. The vertical dashed lines represent the input coupler values used for each cavity. In this case, the cavities are considered to both be under-matched. Experimentally there are reasons for under-matching. When mirrors are coated to reflect certain wavelengths, there is some uncertainty in their reflectivity, up to $\pm 0.5\%$. Additionally, here the loss from the SHG conversion has not been taken into account, which will shift these plots to be closer to the impedance matched case. If the mirror results in having a higher reflectivity, leading to an over-matched cavity, the circulating intensity falls off very quickly, and the cavity may no longer produce the desired enhancement.

Another approach to consider is what happens to the circulating intensity for a fixed r_1 and varying r_m. This relationship can be seen in Fig. 3.3b. Once again both the LBO and BBO have been considered separately, as their input couplers have different reflection coefficients. Here it is clear that regardless of the input coupler, less loss through the rest of cavity will always result is a higher intensity, since the cavity will leak less light through the mirrors. Comparing these two methods for changing optical properties of the cavity, Fig. 3.3a gives the more descriptive representation

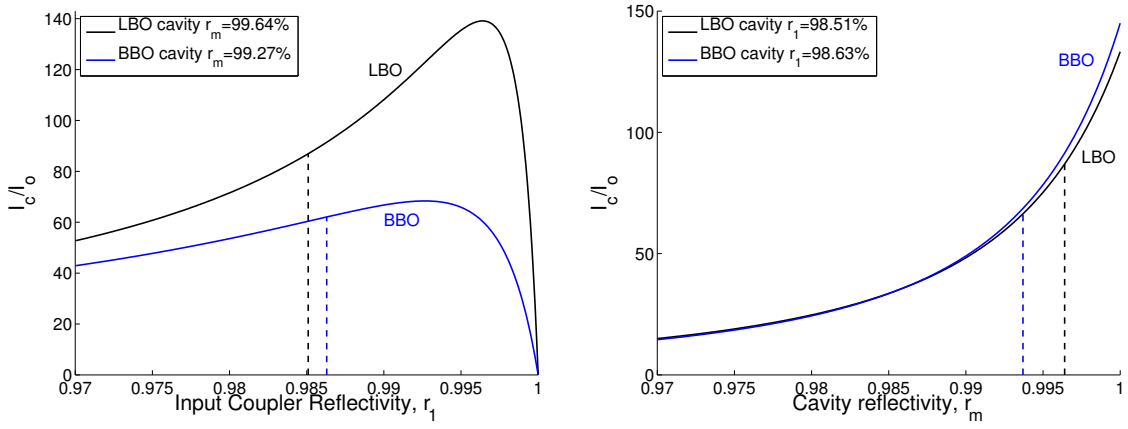

(a) **(b)**

Figure 3.3: Circulating cavity intensity for impedance matching. **(a)** For a varying input coupler reflectivity and constant cavity loss, where the r_m is the reflectivity's of the other cavity mirrors as well as scattering loss through the nonlinear crystals, 0.3% through the LBO and 0.5% through the BBO. The losses due to SHG are not accounted for here. **(b)** A varying cavity loss, r_m, and constant input coupler, for an $r_1 = 98.51\%$ for the LBO cavity and $r_1 = 98.63\%$ for the BBO cavity.

of where a cavity lies with respect to the impedance matched case and how much a cavity can be expected to enhance the light.

3.2 Spatial Mode of Enhancement Cavities: Mode Matching

The basic properties of an enhancement cavity have been discussed in the previous section, including topics of FSR, linewidth and impedance matching. The next topic to discuss is spatial *mode matching*. This is the process of matching the spatial mode of the input light to the spatial mode of the optical cavity. When a laser is mode matched into a cavity most of the input light is coupled into the fundamental spatial mode, TEM_{00}, resulting in a higher intensity in that mode. When the mode matching, or coupling, is poor the intensity will be distributed across many spatial modes. The maximum possible intensity is determined from impedance matching, as discussed in Section 3.1.2 and shown in Fig. 3.3a. To maximize on the available intensity in the TEM_{00} mode, the cavity needs to be spatially mode matched.

There are several pieces to the mode matching puzzle, including the stability of the cavity, the beam profile throughout the cavity, the beam profile of the laser and then the process of matching the spatial mode of the laser to the spatial mode of the cavity. First, the cavities used in this experiment are symmetric bow tie cavities consisting of four mirrors. A schematic of this configuration can be seen in Fig. 3.4. The bow tie cavity is commonly used for generating one directional SHG using nonlinear optics and does not create standing waves in the crystal, like the two mirror Fabry-Perot cavity. In the case of this experiment it is desired to have one beam of second harmonic light with

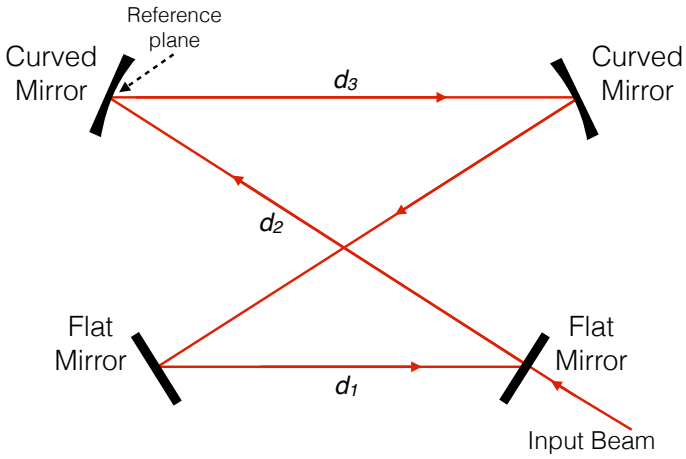

Figure 3.4: Schematic of a ring, or bow tie, cavity configuration. Two of the mirrors are curved and two are flat. The beam travels in one direction around the cavity. The distance between the mirrors are labeled as d_1, d_2 and d_3.

maximum power, rather than two beams. Therefore, the ring cavity is used and not the Fabry-Perot cavity geometry.

3.2.1 Establishing the Mode of the Enhancement Cavity

An optical cavity requires that the spatial mode is stable in order for the light to resonate within the cavity. An unstable cavity means the spatial mode inside the cavity is unable to be replicated after one round trip. Thus the light would eventually leave the cavity and prevent intensity build-up and enhancement of the light in the cavity. Details of stability and how to mathematically determine stability can be found in various textbooks including those by Nagourney and Saleh, [22] and [28] respectively. Stability can also be confirmed using the computer program WinLase© which allows the user to build the optical cavity in the desired geometry. One parameter is varied, for example the distance between two of the mirrors, to show where the cavity is stable as a function of that parameter. WinLase© then plots the beam radius throughout the cavity for the TEM_{00} mode. This information is very important for matching the spatial mode of the laser to the spatial mode of the cavity, as described in more detail in Section 3.2.2. It is also simple to calculate the spatial mode profile of the cavity using the ABCD matrix for one round trip through the cavity for the desired

TEM_{00} cavity mode. This is given by,

$$\begin{pmatrix} A & B \\ C & D \end{pmatrix} = \begin{pmatrix} 1 & 0 \\ \frac{-2}{R} & 1 \end{pmatrix} \begin{pmatrix} 1 & d_1+2d_2 \\ 0 & 1 \end{pmatrix} \begin{pmatrix} 1 & 0 \\ \frac{-2}{R} & 1 \end{pmatrix} \begin{pmatrix} 1 & d_3 \\ 0 & 1 \end{pmatrix}, \tag{3.6}$$

where R is the radius of curvature of the mirrors, and d_1, d_2 and d_3 are the distances between cavity mirrors, as shown in Fig. 3.4. The bow tie cavity has two foci, one between the two flat mirrors and one between the two curved mirrors, where the latter is a tighter focus to optimize the SHG. A complete definition and derivation of the ABCD matrix can be found in any introductory optics textbook [28].

3.2.2 Coupling the Input Beam into the Cavities

In order to match the input light into a cavity, it is crucial to know the spatial beam profile of the fundamental beam itself. The OPSL is a standing wave cavity with one flat mirror and one concave mirror. The flat mirror is at the back of the cavity and the curved mirror is the output coupler. The focus of the beam in the OPSL is at the flat mirror and diverges out to the output coupler. The beam continues to diverge as a spherically symmetric Gaussian beam. The basic Gaussian beam properties can be easily found in an introductory optics textbook [28], however, it is still important to define a few of the key Gaussian beam properties. First, is the beam radius, w, as a function of distance, z, given by,

$$w(z) = w_0 \left[1 + \frac{\lambda z}{n\pi w_0^2} \right]^{1/2}, \tag{3.7}$$

where w_0 is the beam radius at the waist when $z = 0$, λ is the wavelength of the propagating beam and n is the index of refraction. Next is the q parameter, or complex beam parameter, which is used to describe a beam at any point in space. At the beam waist q is given by,

$$q_0 = i\frac{n\pi w_0^2}{\lambda} \tag{3.8}$$

The q parameter can also be written for the beam as it propagates for some distance, z, simply by adding a real term to q_0 to get,

$$q(z) = q_0 + z. \tag{3.9}$$

Using the ABCD matrix the q parameter can be easily transformed as the beam propagates along some distance or through a lens. This simple transformation equation from q_1 to q_2 is given by,

$$q_2 = \frac{Aq_1 + B}{Cq_1 + D}. \tag{3.10}$$

It is important to note that when the light is propagated through a lens, the thin lens approximation is used. This approximation treats the refraction of light through the glass as it enters and exits the material as just the light bending once due to the curvature of the lens. Therefore it is said the light

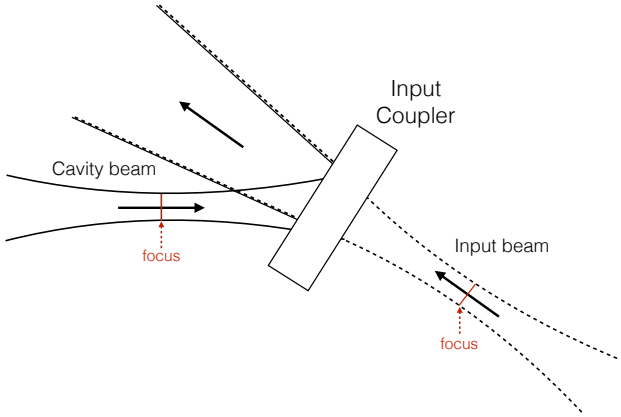

Figure 3.5: Schematic of the spatial mode of the input light coupled to the loose focus and divergence of the enhancement cavity spatial mode. The focus of the input beam matches the focus inside the cavity, and the divergence is the same as the beams meet at the input coupler and propagate to the next mirror.

bends at the centre axis of the lens.

The beam profile for the OPSL can be calculated using theory, but this comes with some assumptions. Namely, the assumption that the beam is Gaussian. To test if the beam is in fact Gaussian and follows as the theory predicts, it is simple to measure the profile of the beam with a CCD camera. The light is focused down through a lens, followed by measurements of the beam radius around the focus. This data is then fit to Eq. 3.7 with one modification,

$$w(z) = w_0 \left[1 + \frac{M^2 \lambda z}{n \pi w_0^2} \right]^{1/2}. \tag{3.11}$$

An added factor has been included, known as the M^2 parameter. This parameter is used to determine how Gaussian the beam is. For a perfectly Gaussian beam, $M^2 = 1$ and for a non Gaussian, $M^2 > 1$. The OPSL was found to have an $M^2 = 1.14$, which shows that the beam is indeed not perfectly Gaussian, but this is still very good. For comparison, a collimated TEM_{00} diode-laser usually has a $M^2 \approx 1.1 - 1.7$ [28]. It is easy to accommodate for an M^2 close to one, by simply multiplying the wavelength by M^2 in the formulas for Gaussian beam propagation as in Eq. 3.11.

As mentioned, the goal of matching the primary beam to the spatial mode of the LBO and BBO cavities is to couple the light to the TEM_{00} mode and maximize the intensity in that mode. The basics of mode matching include using free space and lenses to change the beam shape and size. There are two foci in the ring cavity, one through the nonlinear crystal between the two curved mirrors and one between the two flat mirrors. The one that goes through the crystal is a tight focus with a Rayleigh range that is approximately the length of the crystal to maximize SHG. As a result,

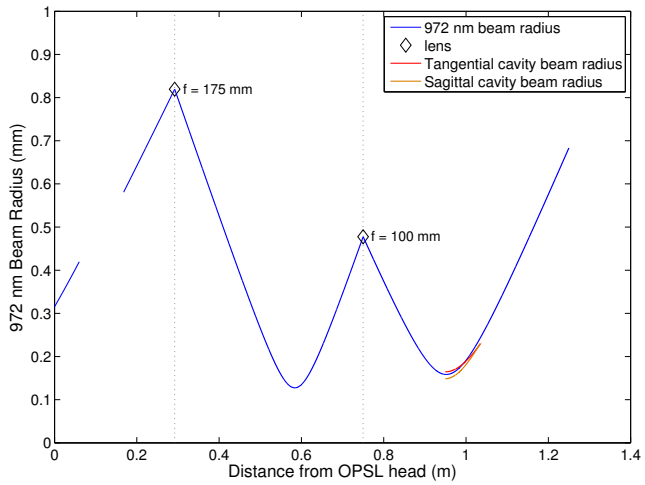

Figure 3.6: Beam radius of the 972 nm laser mode matched into the LBO cavity, where the lenses used to mode match the beam are given as diamonds with their focal lengths labeled. The orange and red lines represent the sagittal and tangential spatial mode of the cavity, from the loose focus to the first curved mirror.

the focus between the two flat mirrors is a looser focus. The beam then diverges from the loose focus and reflects off the input coupler until it reaches the first curved mirror, which causes it to then tightly focus. For mode matching, the input beam is matched to the loose focus and divergence of the beam at the input coupler. If the incoming beam has a similar radius right before it enters into the cavity and diverges at the same angle as the cavity profile, the light should couple well. A schematic of this can be seen in Fig. 3.5, where only the beam around the input coupler is shown in and out of the cavity.

When mode matching the beam into the two enhancement cavities, ABCD matrices are used to propagate the beam from the laser head through the optics until it reaches the first enhancement cavity. In the following sections the beam radius is plotted before each cavity to illustrate how the beam is shaped to get good coupling into each of the cavities.

Mode Matching to the LBO Cavity

Once the beam from the OPSL was determined with the corresponding $M^2 = 1.14$, the beam is propagated through several optics using ABCD matrices, including lenses to focus the beam into the first enhancement cavity, containing the LBO nonlinear crystal. Fig. 3.6 shows the beam radius from the OPSL to the LBO cavity.

The gap in the beam radius is simply where the optical isolator (OI) is located. The red curves are the tangential and sagittal beam radius[1] of the loose focus inside the LBO cavity between the two

[1]The tangential plane is the plane where the optical plane makes an angle with respect to the beam axis. The sagittal plane is perpendicular to the tangential plane. In the case for both the LBO and BBO enhancement cavities, the tangential

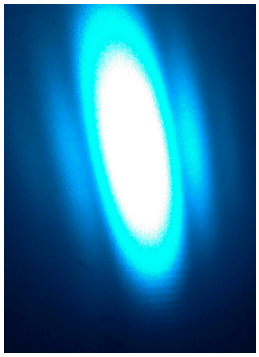

Figure 3.7: Picture of the 486 nm light as it propagates far from the LBO SHG cavity. It can be seen that the beam is in the TEM_{00} mode. The beam diverges at a larger angle in the vertical direction than the horizontal, producing the ovular beam shape.

flat mirrors. As mentioned, this is what the input beam mode is matched too. Since the tangential and sagittal beam was not considered separately for the input light and the difference is minimal inside the cavity, it was decided to match the beam in-between the two curves. The mode matching into the LBO cavity resulted in 74.0% coupling. This result is further discussed in Chapter 4.

Mode Matching to the BBO Cavity

The mode matching to the second enhancement cavity is similar to the LBO with a few additional considerations. The light emitted from the LBO cavity is the second harmonic light, so 486 nm from the fundamental 972 nm. The light is generated in the LBO crystal and propagates out from the crystal through the curved mirror, not following the spatial mode of the cavity. The first thing to notice is that the beam is not spherically symmetric. Fig. 3.7 is a picture of the beam far from the cavity. By focusing this beam through a lens and measuring the beam profile for the horizontal and vertical directions separately and fitting each to Eq. 3.11, the beam is found to be nearly Gaussian in both directions, where $M^2_{horizontal} = 1.02$ and also $M^2_{vertical} = 1.02$.

The 486 nm light is nearly Gaussian, but is still not spherically symmetric and is astigmatic, so each component needs to be mode matched separately. Fig. 3.8 shows the two components, where green is the vertical beam radius and blue is the horizontal. The methods are the same as with the first enhancement cavity, by using ABCD matrices through lenses to match to the spatial cavity mode. Except this time cylindrical lenses are used to isolate the beam shaping in the vertical and horizontal directions. This also allows for matching to the tangential and sagittal conditions of the cavity separately for better mode coupling.

Similarly to the LBO, the results of the mode matching to the BBO cavity were found to have a coupling of 83.6%, which is later discussed in Chapter 4 through experimental and theoretical methods.

plane is parallel to the table.

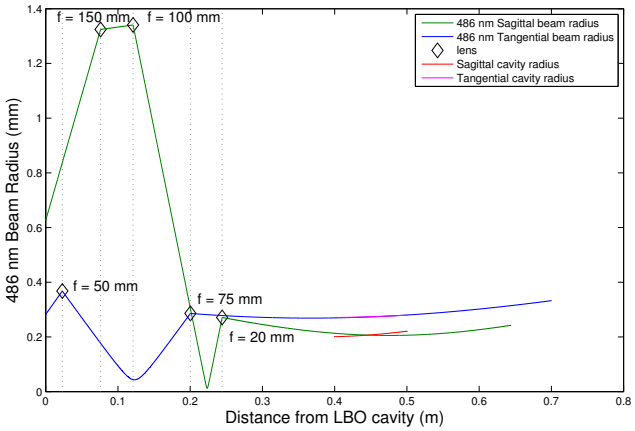

Figure 3.8: Beam radius of the 486 nm laser mode matched into the BBO cavity. The lenses used to mode match the beam are given as diamonds with their focal lengths labeled. The orange and red lines represent the sagittal and tangential spatial mode of the cavity, from the loose focus to the first curved mirror. The green and blue represent the horizontal and vertical spatial modes matching individually using cylindrical lenses.

3.3 Locking the Enhancement Cavities using Pound-Drever-Hall Scheme

The Pound-Drever-Hall locking schemes description starts with a discussion of the reflection signal off the input coupler of the enhancement cavity. Similar to the discussion in Section. 3.1 regarding the circulating intensity inside the cavity, the reflection off the input coupler is now considered. The fractional intensity is given by,

$$\frac{I_r}{I_0} = \frac{(r_1 - r_m)^2 + 4r_1 r_m sin^2(\delta/2)}{(1 - r_1 r_m)^2 + 4r_1 r_m sin^2(\delta/2)}, \tag{3.12}$$

where r_1 is the field reflection coefficient from the input coupler, r_m is the remaining reflectivity's of the cavity mirrors and also includes extra losses due to scattering in the cavity [22]. The round trip phase is given by, δ. Eq. 3.12 plotted as a function of the round trip phase gives Fig. 3.9.

The intensity in the reflected signal is high except for specific values of the round trip phase. Just like in Fig. 3.2 where their were peaks in intensity, the intensity in the reflection dips. This is when the phase difference between the input field and the field inside the cavity after one round trip is a minimum. The electric field components of the reflected signal destructively interferes with the small amount of leakage of the circulating light through in input coupler, causing the intensity to dip [5]. In an ideal case, the reflection dips would go to zero on resonance[2].

The reflection signal can be used to force the laser cavity to stay on resonance, this is called

[2]A zero electric field only results when the laser is perfectly mode and impedance matched. Experimentally the goal is to get the dips as close to zero as possible.

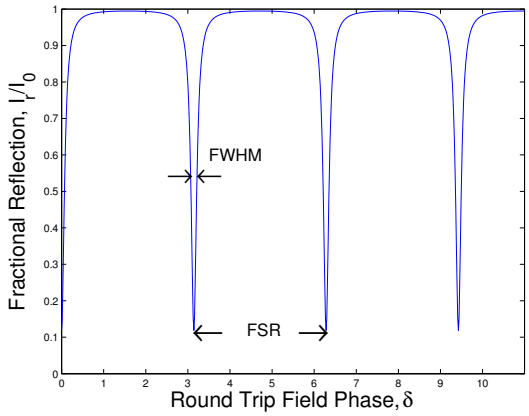

Figure 3.9: Intensity profile of the reflection off the resonator cavity. The full width at half maximum, FWHM, is shown as the width of the absorption lines and the spacing between the peaks are labeled as the free spectral range, FSR. The reflection shows maximum intensity until the cavity is on resonance and then the intensity dips due to the destructive interference of the electric field at the input coupler.

locking. This means that cavity length is locked such that the circulating power is a maximum and the reflected power a minimum for an extend amount of time. This is very important to the SHG to maximize the power in the conversion. The locking scheme used in this experiment is known as the Pound-Drever-Hall, PDH, approach. This method for locking was first developed by Pound in 1946 [23] for microwaves. It was not until 1983 when Drever *et al.* adapted the method for the optical domain [10] to provide laser stability. It is also important to mention that there are two ways to perform this PDH locking scheme. The classical way is for the laser to be locked to a Fabry-Perot cavity with a fixed length. This method stabilizes the laser frequency to match the cavity length and is used in Chapter 5 for measuring the linewidth of the laser. The other method, which is used for the enhancement cavities, is locking the cavity to the laser. In this case there is a PZT inside the enhancement cavities that is locks the length of the cavity to the laser frequency. For any drift in the laser, the PZT changes the length of the cavity to compensate. Before diving into the full explanation of the PDH scheme, it must be established why the PDH approach was chosen over other approaches.

A schematic of the optical and electrical signals used to achieve the PDH locking scheme are shown in Fig. 3.10. The alternating current (AC) signal from the photodiode, where the reflection intensity is measured, enters the mixer as the RF signal. The modulation frequency is split into two signals. One signal goes into the phase modulator to modulate the carrier frequency of the fundamental beam and the other signal is sent through a phase shifter and into the local oscillator (LO) input of the mixer. The phase shifter allows for tuning of the phase between the RF and LO signals to ensure a zero phase shift. The importance of the phase shifter is explained a little later. This is important to the error signal and to the linearity around the zero-zero crossing, as will be also be described more later. The mixer generates the error signal seen in Fig. 3.12. This signal is

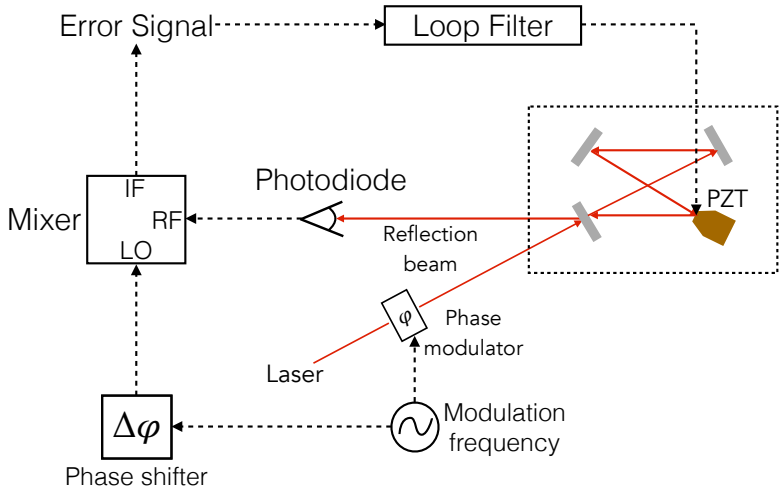

Figure 3.10: A schematic of the electronics for the Pound-Drever-Hall locking scheme. The laser beam is modulated by the phase modulator at a frequency, Ω_m. The reflection beam off the cavity input coupler is propagated onto a photodiode. This signal is then sent into the mixer as an RF signal. A second branch of the modulation frequency is sent through a phase shifter, $\Delta\phi$, and into the local oscillator side of the mixer. The output gives the error signal. This is then sent into the controller, or loop filter and used to control the PZT in the cavity.

then sent into a servo, where the control system uses the zero-zero crossing to lock the cavity to the laser frequency. The output signal from the servo, or loop filter as labeled in Fig. 3.10, is fed back to the enhancement cavity PZT where the cavity length is adjusted to push the phase difference back to zero on the error signal.

In the case of this experiment, the reflected light off the cavity is detected on a photodiode. When the intensity of the light changes, the photodiode converts this into a change in voltage. This signal is sent from the photodetector to a control system that uses feedback to control the length of the cavity. The servo can then simply change the voltage on the PZT to maintain the minimum power on the photodetector. A change in reflected power could have a number of causes, one because the cavity is off resonance and therefore there is some overall intensity change, or simply because the power in the laser changed. Assuming it is the first reason, the intensity would change the same amount on either side of the resonance, above or below. The photodetector sends this higher voltage signal to the servo, which then determines that the cavity is off resonance. Since the signal appears the same above and below resonance the electronics are unable to determine in which direction the cavity length is off. The electronics might push the cavity length in the correct direction, or push it even farther off resonance. In order for the electronics to accurately determine if the cavity is above

or below resonance, it would have to distinguish the phase from the intensity. Currently there are no electronics that can do this [5]. Another possible locking scheme involves locking to the side of a resonance peak, however since the lock is not at the peak of the resonance, it is not possible to lock to the highest possible power in the cavity.

The ability to use changes in phase is what makes the PDH scheme so stable and a desirable approach to locking. To determine the phase of the reflected signal, the phase of the carrier, or laser, frequency is modulated. This is known as the modulation frequency, Ω_m, and is usually larger than the linewidth of the enhancement cavity that is being locked to the laser. For this experiment the modulation frequencies are $\Omega_m = 14$ MHz for the LBO cavity and $\Omega_m = 10$ MHz for the BBO cavity. This modulation is applied by passing the laser light through a phase modulator. Typically, a laser is only modulated at one frequency, however, for this experiment each enhancement cavity requires its own modulation frequency. To do this, an adding step up transformer is used to combine the two frequencies that puts the corresponding phase modulations on the carrier frequency, as can be seen in the original schematic in Fig. 2.1.

Next, it is useful to jump ahead to Fig. 3.12 to conceptually understand the benefit and the stability of the the PDH scheme. This figure shows the PDH error signal at high modulation frequencies, in the range of MHz. The zero-zero crossing of the signal is the position where the cavity is on resonance with the laser. The slope of the line crossing through zero is both very steep and with high amplitude. When the cavity is slightly detuned from resonance, the signal on the photodiode will contain some component of the modulation frequency and therefore a change in the phase. This will cause a corresponding change along the error signal, either in the positive or negative direction. This change in voltage will then cause the servo to apply a feedback voltage back on the cavity PZT to drive the phase shift back to zero.

To mathematically describe how to arrive at the high modulation frequency PDH error signal, start with the unmodulated electric field of the input beam,

$$E(t) = E_0 e^{-i\phi(t)} = E_0 e^{-i\omega_c t}, \tag{3.13}$$

where E_0 is the amplitude of the field, $\phi(t)$ is the time-dependent phase, and ω_c is the carrier frequency. A time-dependent phase modulation, given by $\Delta\phi(t)$, is then applied to the carrier frequency. $\Delta\phi(t)$ can be written as $\beta \sin\Omega_m t$, where Ω_m is the modulation frequency and the modulation depth is given as β and determines the amplitude of the modulation. For the sake of this derivation, only one phase modulation will be applied to the carrier frequency. This derivation can simply be expanded to account for the two modulations that are actually applied in the experiment, one for each enhancement cavity. The modulated field then becomes,

$$E(t) = E_0 e^{-i(\phi(t)+\Delta\phi(t))} = E_0 e^{-i(\omega_c t+\beta \sin\Omega_m t)}. \tag{3.14}$$

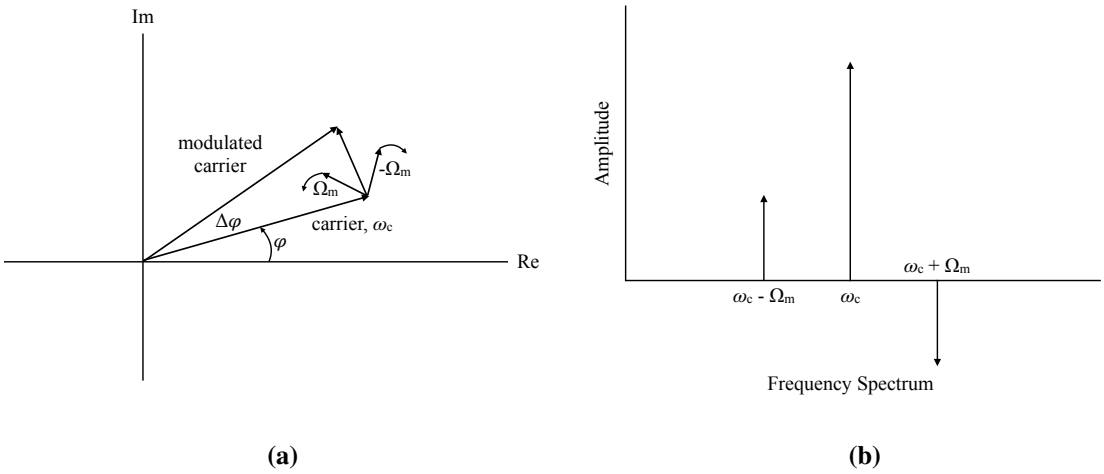

Figure 3.11: Representation of the phase and amplitude under phase modulation. **(a)** Is the phasor diagram on the real and imaginary axes. The carrier frequency, ω_c rotates with phase, ϕ. The modulated carrier is phase shifted by $\Delta\phi$ from the carrier frequency by a modulation frequency of Ω_m. **(b)** Is the amplitude of the carrier frequency with phase shifted sidebands at frequencies $\omega_c \pm \Omega_m$.

This can then be expanded using Bessel functions to the first order, with small β,

$$E(t) \approx E_0[J_0(\beta)e^{-i\omega_c t} + J_1(\beta)e^{-i(\omega_c+\Omega_m)t} - J_1(\beta)e^{-i(\omega_c-\Omega_m)t}], \tag{3.15}$$

where $J_0(\beta)$ and $J_1(\beta)$ are the Bessel function coefficients [15]. From Eq. 3.15 it is clear to see that there are in fact three terms to the electric field contributed by the phase modulation. These $J_1(\beta)$ terms are knows as the sidebands as shown in Fig. 3.11b. Once again, β is the modulation depth. For $\beta < 1$ almost all of the power is in the carrier frequency and the first order sidebands [5]. Due to the phase modulation, one sideband is 180^o out of phase with the other one. This is actually a key component to how PDH lock works, being able to discriminate which direction the resonance is off by the sign due to the sideband.

Taking a closer look, Fig. 3.11 can give more conceptual understanding before evaluating the mathematics any further. Fig. 3.11b shows the amplitude plot of the carrier frequency and sidebands. This is not the absolute amplitude so that it can clearly be seen that the two sidebands are 180^o out of phase with each other. The two sidebands are rotating in opposite directions, so the sum of the amplitudes remains constant. Fig. 3.11a shows the phasor representation of the carrier frequency and two sidebands. Here the carrier frequency remains constant, rotating at ω_c, while the modulation frequencies rotate creating a new vector, called the phase modulated carrier frequency. This vector has a phase shift of $\Delta\phi$ from the carrier frequency. This phase shift changes as the modulation frequencies rotate.

Continuing with the mathematical derivation of the error signal, the reflected light can be written in terms of the electric field of the incident light and the reflection coefficient, $F(\omega)$. The reflection

coefficient is simply the ratio of the reflected electric field to the incident electric field at a given frequency, ω,

$$F(\omega) = \frac{E_{refl}}{E_0} = \frac{r\left(e^{i\omega/\Delta\nu_{FSR}} - 1\right)}{1 - r^2 e^{i\omega/\Delta\nu_{FSR}}}. \tag{3.16}$$

The amplitude reflection coefficient is r and $\Delta\nu_{FSR}$ is the FSR [5]. Eq. 3.15 can then be written as,

$$\begin{aligned} E_{refl} = E_0[F(\omega_c)J_0(\beta)e^{-i\omega_c t} + F(\omega_c+\Omega_m)J_1(\beta)e^{-i(\omega_c+\Omega_m)t} \\ -F(\omega_c-\Omega_m)J_1(\beta)e^{-i(\omega_c-\Omega_m)t}]. \end{aligned} \tag{3.17}$$

The next stage is to transform the reflected electric field into a power, as that is what the photodetector measures. The relationship between power, P and electric field, E, is simply $P = |E|^2$. Therefore, Eq. 3.17 can be written as,

$$\begin{aligned} P_{refl} = P_c|F(\omega_c)|^2 + P_s|F(\omega_c+\Omega_m)|^2 + P_s|F(\omega_c-\Omega_m)|^2 \\ +2\sqrt{P_c P_s}\{Re[F(\omega_c)F^*(\omega_c+\Omega_m) - F^*(\omega_c)F(\omega_c-\Omega_m)]\cos\Omega_m t \\ +Im[F(\omega_c)F^*(\omega_c+\Omega_m) - F^*(\omega_c)F(\omega_c-\Omega_m)]\sin\Omega_m t\} \\ + \textit{higher order terms}, \end{aligned} \tag{3.18}$$

where P_c is the carrier power and P_s is the sideband power [5]. This equation simplifies depending on the modulation frequency. For the case of this experiment, the modulation frequency is high, meaning $\Omega_m \gg \Delta\nu_{fsr}/\mathcal{F}$, where $\Delta\nu_{fsr}/\mathcal{F}$ is the linewidth of the cavity. Only the sine term remains, while the cosine term vanishes [5].

This RF signal is fed into the mixer where it is mixed with the original modulation frequency. In the mixer, the inputs are multiplied together. Thus, the product of two sine waves will give a cosine of the sum and difference term of the phase shift between the input waves. Similarly, if one input is a sine and the other a cosine, the product is the sine of the sum and difference of the phase shift [5]. When the phase between the RF and LO signal is the same, the result is a direct current (DC) plus AC term for the two sine waves and only an AC term for the sine and cosine inputs. This AC term is the error signal. The phase of the modulation frequency can simply be adjusted to make this scenario true by running the signal through a phase shifter before the mixer.

For high modulation frequency, as used in this experiment, the error signal is given by,

$$\varepsilon = -2\sqrt{P_c P_s}Im[F(\omega_c)F^*(\omega_c+\Omega_m) - F^*(\omega_c)F(\omega_c-\Omega_m)], \tag{3.19}$$

and produces the signal shown in Fig. 3.12. For the point where the cavity is on resonance with the laser carrier frequency, the error signal crosses zero and is nearly linear. Further simplification can be done to reduce the analysis around this point.

When the carrier frequency is at or near resonance, the sidebands are far enough away that their power is completely reflected, or $r \approx 1$. This results in the sideband reflection coefficients from

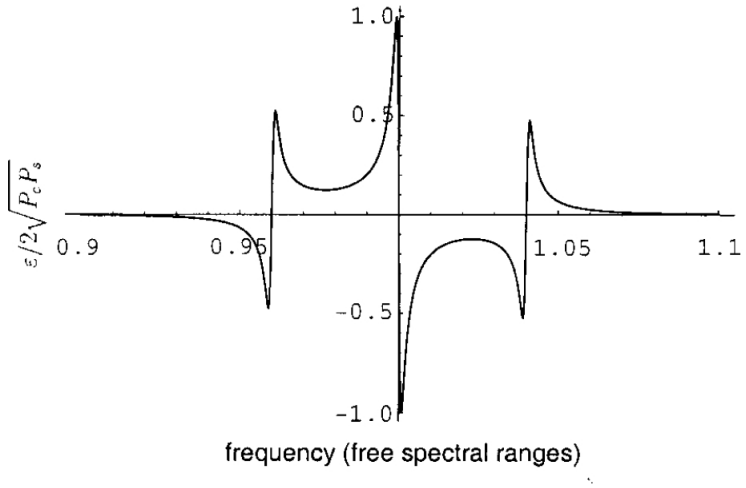

Figure 3.12: The PDH error signal after the reflection signal from the cavity is converted to an RF signal and mixed with the original phase modulation signal. When the phase between the two mixed signals is the same, the above error signal is produced. Plot produced by Black [5].

Eq. 3.16, $F(\omega_c \pm \Omega_m) \approx -1$. Thus, reducing Eq. 3.18 to,

$$P_{refl} \approx 2P_s - 4\sqrt{P_c P_s} Im\{F(\omega_c)\} \sin\Omega_m t + \textit{ higher order terms}. \tag{3.20}$$

The error signal also simplifies to,

$$\varepsilon = 4\sqrt{P_c P_s} Im[F(\omega_c)]. \tag{3.21}$$

The reflection coefficient from Eq. 3.16 can be approximated for the carrier frequency, so that it does not go to zero. Exactly on resonance $\frac{\omega}{\Delta\nu_{FSR}} = 2\pi N$, where N is an integer number and $e^{i2\pi N} = 1$, so $F(\omega_c) = 0$. Thus, $\frac{\omega}{\Delta\nu_{FSR}}$ is instead replaced by,

$$\frac{\omega}{\Delta\nu_{FSR}} = 2\pi N + \frac{\delta\omega}{\Delta\nu_{FSR}}, \tag{3.22}$$

where $\frac{\delta\omega}{\Delta\nu_{FSR}}$ is some small offset from resonance. The finesse of the cavity can also be approximated as $\mathcal{F} \approx \pi/1-r^2$, when $r \approx 1$, and the linewidth is $\delta\nu = \Delta\nu_{FSR}/\mathcal{F}$. For an offset frequency, $\delta\omega$, much less than the linewidth, $\delta\nu$, and after some substitution and simplification, the reflection coefficient of the carrier frequency is approximated to,

$$F(\omega_c) \approx \frac{i}{\pi}\frac{\delta\omega}{\delta\nu}. \tag{3.23}$$

The error signal becomes,

$$\varepsilon \approx -\frac{4}{\pi}\sqrt{P_c P_s}\frac{\delta\omega}{\delta\nu}. \tag{3.24}$$

Now, it is clear to see that the error signal is linear around resonance for small deviations in the phase, or frequency. This is beneficial to the stability of the lock because a small change in phase, translates directly to a small change in the error signal and then the servo can linearly respond to the PZT. If the error signal was not linearly proportional around zero-zero, then the feedback loop may over compensate or add additional noise to the lock, resulting in a less stable lock.

Chapter 4

Nonlinear Optics and Second Harmonic Generation

The focus of this chapter is specifically on the second harmonic generation, SHG, process using nonlinear optics through the two optical enhancement cavities. The last chapter detailed the basics of the optical cavity and how to experimentally match the fundamental spatial mode to the cavity mode. This chapter will explain the theory and experimental results of using nonlinear optics inside the enhancement cavities, starting with the basics in Section 4.1. This section will cover the different crystal types used in this experiment and their geometrical symmetries. Then Section 4.1.1 presents the theory for the nonlinear conversion factor, γ_{SH}, and the Boyd-Kleinman parameter. Finally the theory and experimental results for the conversion from the input light into the enhancement cavity to the second harmonic generated light are presented in Section 4.2. The comparison of the theory to experimental data gives a measure for how well the cavities where impedance and mode matched from Chapter 3.

4.1 Nonlinear Crystal Symmetry Basics

The uses of nonlinear crystals varies widely across the field of optics, from second and third harmonic generation to frequency mixing. Nonlinear crystals have three main symmetries, uniaxial, biaxial and isotropic. In this experiment only uniaxial and biaxial are used, so the discussion will be focused on these two types. Uniaxial and biaxial refers to the number of optical axis that are in the crystal as well as the indices of refraction along the x, y and z axes. The optical axis, or c-axis, is defined as the axis along which a beam would experience no birefringence or double refraction. Table 4.1 shows the relative indices of refraction, n, for the uniaxial and biaxial crystal, for both positive and negative types. The uniaxial defines the x, y and z in terms of just two values, the ordinary and extraordinary, denoted as o and e respectively. This is simply because two of the axes have the same index of refraction. The relative values of n for the biaxial crystal remain such that $n_z > n_y > n_x$ for both the positive and negative types. The positive and negative biaxial types come from how the two optical axes are oriented in the $x-z$ plane. Fig. 4.1 illustrates the positive and

	Uniaxial	Biaxial
Positive	$n_z = n_e > n_x = n_y = n_o$	$n_z > n_y > n_x$
Negative	$n_x = n_y = n_o < n_z = n_e$	$n_z > n_y > n_x$

Table 4.1: The relationship of the indices of refraction of the uniaxial and biaxial crystals along the x, y and z axes, for the positive and negative orientations. The uniaxial is also described by ordinary, o, and extraordinary, e, axes. The relationship of n for the biaxial crystals is the same for both positive and negative symmetries.

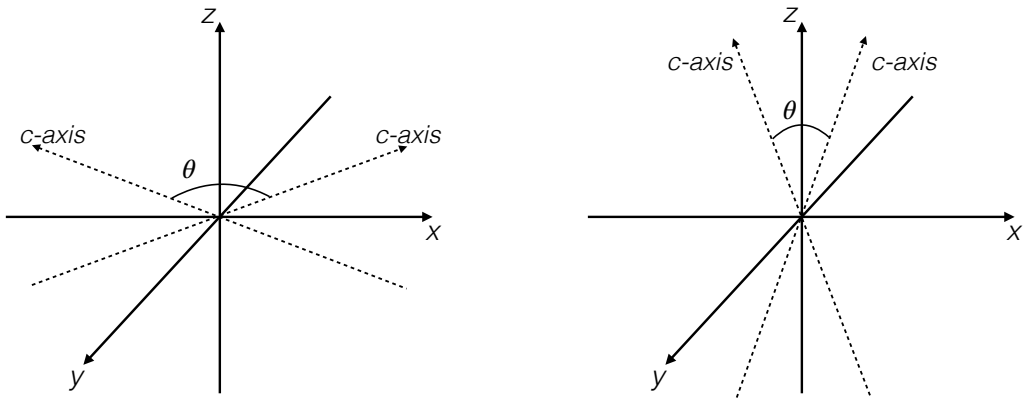

(a) Positive Biaxial **(b)** Negative Biaxial

Figure 4.1: Schematic of biaxial positive and negative symmetries. **(a)** Is the positive biaxial crystal, where the two optical, c-axes are folded around the x-axis and **(b)** a negative biaxial crystal where the two optical, c-axes are folded around the z-axis.

negative orientations of the optical axes for the biaxial crystal. The angle between the two optical axes, θ, is determined by the indices of refraction and is given by,

$$\theta = cos^{-1}\sqrt{\frac{1/n_y^2 - 1/n_z^2}{1/n_x^2 - 1/n_z^2}}. \tag{4.1}$$

When θ is large, the optical axes are closer to the x-axis and referred to as positive biaxial. When θ is small, this is negative biaxial and the optical axes are closer to the z axis. Table 4.1 shows the relationship of the indices of refraction for the uniaxial and biaxial, positive and negative crystal symmetries.

The discussion about the indices of refraction in both crystal symmetries is extensive and most of the information is easily available in various nonlinear optics text books, including Boyd [7] and Nagourney [22]. A brief overview will be given here to preface the next section of second harmonic generation. In 1871 Wilhelm Sellmeier first proposed alternate methods to Cauchy's theory on the index of refraction through a material and how it depends on wavelength. Sellmeier found the

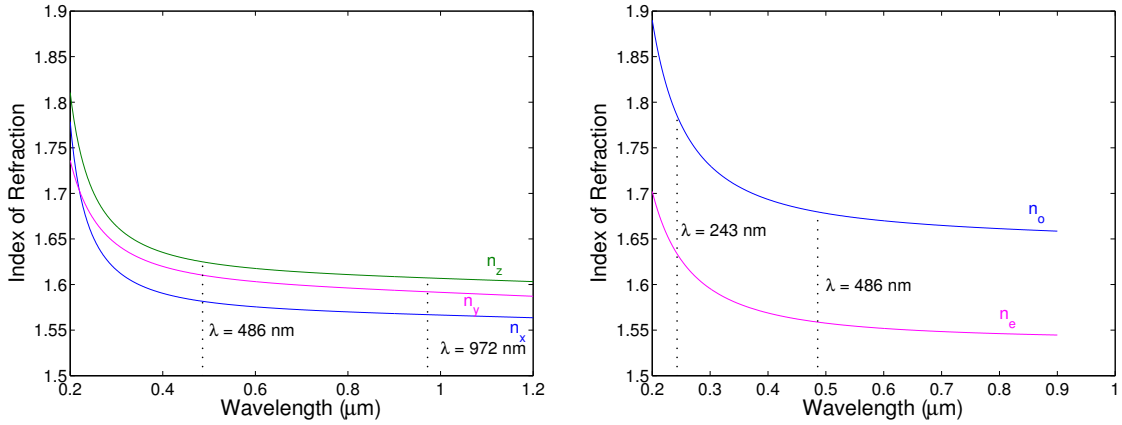

(a) LBO **(b)** BBO

Figure 4.2: Index of refraction curves for changing wavelength, λ, for both LBO and BBO crystals. **(a)** The LBO crystal, where the indices for each axis are shown as well as the wavelength for both the fundamental and second harmonic. **(b)** BBO crystal indices of refraction are shown, for the ordinary and extraordinary axes, as well as the fundamental and second harmonic λ. The coefficients used are the Sellmeier coefficients given in Nagourney [22].

following relationship,

$$n^2 = A + \frac{B\lambda^2}{\lambda^2 - C} + \frac{D\lambda^2}{\lambda^2 - E}, \tag{4.2}$$

where A, B, C, D, and E are Sellmeier coefficients and λ is the wavelength. These coefficients are unique for each material and have been listed in Table 13.1 in Nagourney for both the LBO and BBO crystals [22]. Fig. 4.2 shows Eq. 4.2 for the LBO and BBO cavities, with both the fundamental wavelength and second harmonic wavelength identified. The relationships between the indices of refraction and wavelength conversion are important for the concept of *phase-matching* for SHG.

This experiment uses two nonlinear crystals for SHG inside an enhancement cavity. The first crystal used is the LBO, which is a negative biaxial crystal, and the second is a BBO, which is a negative uniaxial crystal. The beam propagation through the crystal can be defined in terms of two angles, θ_p and ϕ. These are known as the phase-matching angles. The phase-matching angle θ_p is the angle **k** makes with the z-axis and ϕ is the angle from the $x-z$ plane. In order to achieve SHG in a nonlinear crystal, the crystal must be phase-matched. This means that the indices of refraction are the same for the fundamental and second harmonic wavelengths. This can only be achieved for one wavelength if the light is simply propagated long a specific axes, say the z-axis. This is not convenient for all lasers, as the wavelengths desired varies across experiments and there are a limited number of available nonlinear crystals. To remedy this, the fundamental beam can be propagated at some angle relative to the axes, given as either θ_p or ϕ. The angle θ_p is the angle between the optical axis and the direction of beam propagation, $\boldsymbol{k}$, and lies in the $x-z$ plane. The angle ϕ is the azimuthal angle from the $x-z$ plane to the direction of propagation. A basic schematic of the

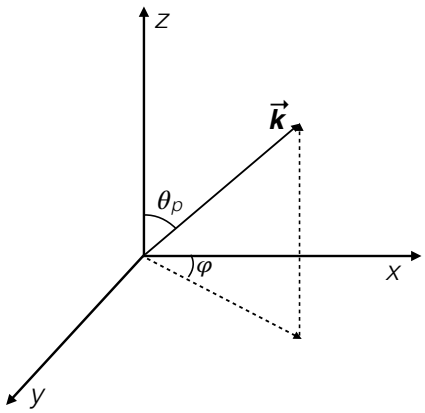

Figure 4.3: Crystal axes with the phase-matching angles, θ_p and ϕ, for a given direction of beam propagation, **k**.

axes, beam propagation direction, **k**, and phase-matching angles are illustrated in Fig. 4.3. For the specific types of crystal used, the uniaxial and biaxial, a schematic of the axes and phase-matching angles can be seen in Fig. 4.4. Each type of crystal has a different critical phase-matching angle. For the uniaxial crystal in Fig. 4.4a, θ_p, is the critical angle and ϕ is arbitrary because the indices of refraction along the x and y axis are the same as defined in Table 4.1. For the biaxial crystal, θ_p is fixed at 90^o so that ϕ becomes the critical phase-matching angle. However, both are important angles to specify when growing the crystals.

The methods for selecting the phase-matching angle are easily described for the uniaxial crystal, but can be applied to the biaxial case in a similar manner. For the negative uniaxial crystal, the fundamental light is the ordinary wave, polarized perpendicular to the c-axis, and the second harmonic would be the extraordinary wave, polarized long the c-axis. When a crystal is phase-matched the index of refraction of the the ordinary wave, n_o, equals the index of the second harmonic extraordinary wave, n_e. From Fig. 4.2 it can be seen that for both the LBO and BBO cases, $n_o^{\nu} \neq n_e^{2\nu}$. The notation ν is used to describe the fundamental and 2ν for the second harmonic of the optical frequency. This discrepancy in indices can be more clearly seen for the BBO crystal, where the n_o at the fundamental, $\lambda = 486$ nm, does not give the same value in n_e at the second harmonic, $\lambda = 243$ nm. If the beam is propagated at some angle, θ_p, relative to the optical axis, then the index of refraction that the beam sees is different. The relationship to describe how the index depends on θ_p can be written as,

$$\frac{1}{(n_e^{2\nu}(\theta_p))^2} = \frac{cos^2(\theta_p)}{(n_o^{2\nu})^2} + \frac{sin^2(\theta_p)}{(n_e^{2\nu})^2}, \tag{4.3}$$

There exits some angle for which the phase-matching condition holds, $n_o = n_{e,}^{2\nu}$. By rewriting

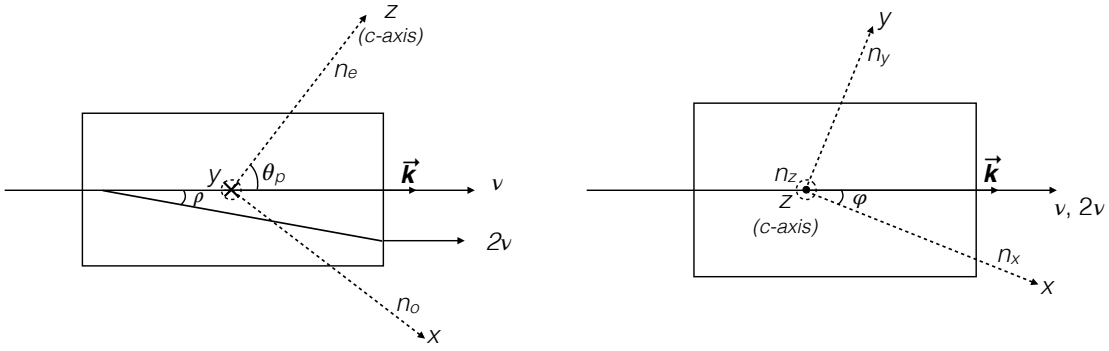

(a) Uniaxial **(b)** Biaxial

Figure 4.4: Schematic of uniaxial and biaxial crystal symmetries. **(a)** The negative uniaxial crystal, as seen from the side view. The direction of propagation, $\boldsymbol{k}$, of the fundamental frequency, ν lies at an angle θ_p from the z-axis. phase-matching angle, $\phi = 0$ as the indices of refraction along the x and y axis are the same, and called the ordinary axis, n_o. The z-axis is the extraordinary axis, n_e, also known as the c-axis. The walk-off angle, ρ is the angle the second harmonic, 2ν, from the fundamental beam, ν. **(b)** The negative biaxial crystal, as seen from the top view. In this crystal the angle $\theta_p = 90^o$, making ϕ the critical phase-matching angle along which $\boldsymbol{k}$ propagates.

Eq. 4.3,

$$sin^2(\theta_p) = \frac{(n_o^{\nu})^{-2} - (n_o^{2\nu})^{-2}}{(n_e^{2\nu})^{-2} - (n_o^{2\nu})^{-2}} \tag{4.4}$$

a value for θ_p can be found for the desired fundamental wavelength. This same relationships can be used in the biaxial crystal cases, where each of the axes exhibit a different index of refraction to find both the value for θ_p and ϕ.

There is another phenomenon that takes place inside the crystal, called double refraction or birefringence. When the second harmonic photons are produced they will propagate at some angle away from the fundamental direction of propagation. This is known as the *walk-off* angle and denoted by ρ. The expression to find this angle is given by,

$$tan(\rho) = \frac{(n_o^{\nu})^2}{2}\left[\frac{1}{(n_e^{2\nu})^2} - \frac{1}{(n_o^{2\nu})^2}\right] sin(2\theta_p), \tag{4.5}$$

where it can be seen that ρ depends on θ_p and on the the indices of refraction seen by the fundamental and second harmonic [17]. A schematic of the walk-off angle and how the second harmonic separates from the fundamental is shown in Fig. 4.4a for the uniaxial crystal.

The BBO, negative uniaxial crystal if found to have a phase-matching angle of $\theta_p = 54.8^o$, with $\phi = 0$ because the index of refraction along the x and y axes are the same, making ϕ a non-critical phase-matching angle. From θ_p, the walk-off angle is found to be $\rho = 4.9^o$. The LBO crystal is

a negative biaxial crystal, with $\theta_p = 90^o$ and $\phi = 17.5^o$. In this case, θ_p is the non-critical phase-matching angle. The walk-off angle is proportional to $sin(2\theta_p)$, so when $\theta_p = 90^o$, $\rho = 0$, so there is no walk-off angle for this crystal.

Finally, the effective nonlinear coefficient, denoted by d_{eff}, is another coefficient used in the description of second harmonic generation. This coefficient is dependent on θ_p, ϕ, ρ and λ. The various crystal symmetries have a basic formula to describe d_{eff} in terms of other tensor coefficients, d_{ij} and θ_p and ϕ [22]. For the BBO,

$$d_{eff} = d_{15} sin\theta - d_{22} cos\theta sin3\phi. \tag{4.6}$$

The tensor coefficients, like d_{15} and d_{22}, are dependant on crystal symmetry, ρ and λ. The best computation of d_{eff} for both the LBO and BBO crystal used at their respective wavelengths is a program called SNLO© [31]. This program considers all of the relevant parameters and corrections to determine the most accurate value for d_{eff}. For the LBO, $d_{eff} = 0.82$ pm/V and for the BBO, $d_{eff} = 1.58$ pm/V.

Understanding the basics of the crystal symmetry is important for continuing the discussion of second harmonic generation and optimizing conversion efficiency from the fundamental to the second harmonic inside the enhancement cavity.

4.1.1 Boyd-Kleinman Nonlinear Conversion Factor

This section will present the theory for the second harmonic conversion factor from the fundamental to the second harmonic through a nonlinear crystal using the previously developed crystal geometries. The derivation of the conversion factor begins with the wave equation for the second harmonic,

$$\frac{\delta E(2(2\pi\nu))}{\delta z} = -\frac{i(2\pi\nu)}{n_{2\nu}c} d_{eff} E(2\pi\nu) E(2\pi\nu) e^{i(k(2(2\pi\nu))-2k(2\pi\nu))z} \text{ [17]}, \tag{4.7}$$

where $n_{2\nu}$ is the index of refraction seen by the second harmonic and d_{eff} is the effective nonlinear coefficient as discussed in the previous section. For the phase-matched condition, the wave numbers, $(k(2(2\pi\nu)) - 2k(2\pi\nu)) = 0$ and the index of refraction is the same for both the fundamental and second harmonic, $n_{2\nu} = n_\nu = n$. Simplifying and differentiating Eq. 4.7 for $z = l$,

$$E(2(2\pi\nu), z = l) = -\frac{i(2\pi\nu)}{nc} d_{eff} E^2(2\pi\nu). \tag{4.8}$$

In terms of the optical intensity,

$$I(2(2\pi\nu), l) = -\frac{2(2\pi\nu)^2 d_{eff}^2}{n^3 c^3 \varepsilon_0} L^2 I^2(2\pi\nu), \tag{4.9}$$

where ε_0 is the permittivity of free space and L is the interaction length, or length of the crystal [17]. From Eq. 4.9 the coefficients in front of the $l^2 I^2(2\pi\nu)$ can be lumped together as a general form for

the second harmonic conversion factor.

Since this experiment deals with a focused Gaussian beam through the nonlinear crystal, the second harmonic conversion factor requires an additional component that depends on the beam shape and size through the crystal. This term has been derived from the well-known Boyd and Kleinman work from 1968 for a focused Gaussian beam [6]. Additionally, it is more convenient to work in terms of power rather than intensity. Then the second harmonic conversion factors from Eq. 4.9 can be written as a single term, γ_{SH}, and given as,

$$\gamma_{SH} = \left(\frac{2(2\pi\nu)^2 d_{eff}^2 k_{(2\pi\nu)}}{\pi n^3 \varepsilon_0 c^3} \right) L h(B,\xi). \tag{4.10}$$

The length of the crystal is given by L, n is the refractive index, d_{eff} is the effective nonlinear coefficient, ν is the fundamental laser frequency, $k_{(2\pi\nu)}$ is the fundamental wave number, c is the speed of light, and ε_0 is the permittivity of free space. The parameter, $h(B,\xi)$ is known as the Boyd and Kleinman focusing factor. It is within this factor that the specifics of the beam interacting within the crystal are important. For a complete derivation of this parameter, see Boyd and Kleinman paper [6]. Throughout the literature there are other approximations for finding $h(B,\xi)$. Two of these methods will be used in this analysis.

It must first be established that $h(B,\xi)$ depends on two parameters, B and ξ. B is the double refraction and ξ is the focusing parameter.

$$B = \rho \left(\frac{\pi L}{2\lambda} \right)^{1/2} \tag{4.11}$$

where λ is the wavelength inside the crystal and L is the length of the crystal [6]. It can be seen that this parameter depends on the walk-off angle. In the case of the LBO crystal, $\rho = 0$, because the non-critical phase-matching angle is 90^o. Thus, $B = 0$ for conversion from 972 nm to 486 nm. For the second conversion stage from 486 nm to 243 nm, using the BBO crystal, $\rho \neq 0$, rather $\rho = 4.9^o$ and thus $B = 19.16$ for a crystal length of 10 mm.

The focusing parameter, ξ, is defined as $\xi = \frac{L}{b}$. Again, L is the length of the crystal and b is the confocal parameter, which is simply two times the Rayleigh length. The Rayleigh length is a characteristic parameter used to describe a Gaussian beam around a focus, and given as

$$z_R = \frac{n\pi w_0^2}{\lambda}. \tag{4.12}$$

In words, the Rayleigh length is the distance it takes the beam to grow by the $\sqrt{2}$, from the waist, w_0. For the fundamental beam focusing through the LBO, $\xi = 0.93$, and for the BBO, $\xi = 0.28$.

To determine $h(B,\xi)$, there are two methods. The first is to simply use Fig. 4.5 from the Boyd and Kleinman paper, where they plot several curves of $h(B,\xi)$ as a function of ξ, for a few values of B. For the LBO, $h(B,\xi) \approx 0.8$, with $d_{eff} = 0.82$ pm/V, leading to a $\gamma_{SH} = 1.19x10^{-4}$. Since Fig. 4.5 does not give a curve for $B = 19$ it is best to use an approximation provided by Nagourney [22].

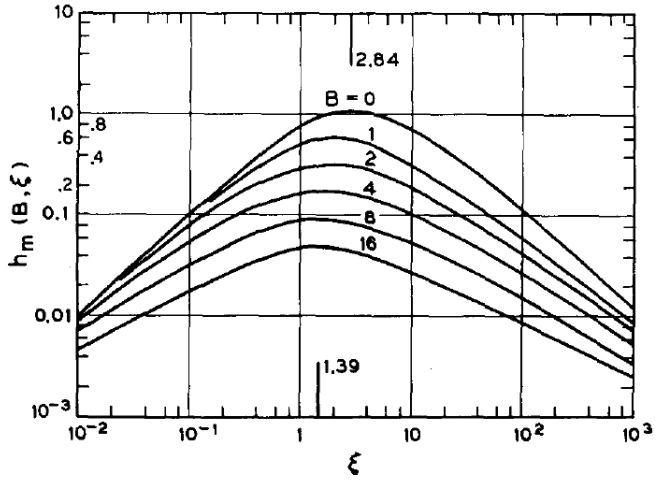

Figure 4.5: Boyd-Kleinman factor as a function of the focusing parameter, ξ, for various values of B, the double refraction parameter. This plot was taken from Boyd and Kleinman (1968), Fig. 2 [6] and is used to approximate a value of $h(B,\xi)$ for a given ξ and B.

This approximation holds when $\xi < 0.4$ and $B > \sqrt{6/\xi}$, and is given by,

$$h(B,\xi) \approx \frac{\sqrt{\pi}\xi^{1/2}}{2B}. \tag{4.13}$$

From this, $h(B,\xi) = 0.024$, and for $d_{eff} = 1.58$ pm/V, $\gamma_{SH} = 8.2x10^{-5}$. The next step now is applying the second harmonic coefficient into the intensity calculations of the enhancement cavity to determine how much intensity is generated in the second harmonic.

4.2 Second Harmonic Generation in an Enhancement Cavity

The single pass efficiency for a CW laser through a nonlinear crystal in the borate family is around 10^{-4} W^{-1} or 0.1% [8]. For this experiment and many others, a higher efficiency is desired. Adding an enhancement cavity around the crystal leads to an efficiency of 30-45%. The theory for the nonlinear optics and conversion from the fundamental beam to the frequency doubled light uses the same optical component parameters as those defined in Chapter 3. The basic theory for understanding and calculating the nonlinear process while the crystal is in an enhancement cavity follows from the work of Kozlovsky, Nabors and Byer (KNB) [19] who nicely compiled the more extensive work of Ashkin, Boyd and Dziedzic (ABD) [2].

As previously defined, the transmission and reflection through the input coupler remain the same, t_1 and r_1 respectively. The definition of r_m is now defined

$$r_m = t^2 t_{SH} r_2, \tag{4.14}$$

where r_2^2 is again the field reflection coefficient from the cavity mirrors, excluding the input coupler, and $t^2 = 1 - losses$. The new t_{SH} term accounts for a depletion of the fundamental light as it is converted to the second harmonic. As long as the loss from the conversion is small,

$$t_{SH}^2 = (1 - \gamma_{SH} P_c), \tag{4.15}$$

where P_c is the circulating power and γ_{SH} is the second harmonic coefficient. Previously, in Chapter 3 intensity was used as the metric for measuring the light in and out of the cavity. Intensity is simply the power per unit area. In this section power will be the metric used.

Recall Eq. 3.5 that related the circulating intensity to the input intensity. Writing this equation in terms of power and substituting Eq. 4.15 into Eq. 4.14 gives the new relation,

$$\frac{P_c}{P_0} = \frac{t_1^2}{(1 - r_1 t^2 r_2 (1 - \gamma_{SH} P_c))^2}. \tag{4.16}$$

From the circulating power there is a simple relationship to find the power produced in the second harmonic and is given by,

$$P_{SH} = \gamma_{SH} P_c^2. \tag{4.17}$$

This relationship is only true for the ring cavity configuration, since the second harmonic is only produced in one direction. The second harmonic coefficient, γ_{SH}, has previously been derived in Section 4.1.1. The next step is to compare the theoretical SHG for given fundamental powers for each the LBO and BBO cavities to experimental results.

LBO

The experimental measurements were taken by measuring the power of the input light right before the cavity and power in the second harmonic as it left the cavity, while the cavity was locked. As can be seen in Fig. 4.6a the theory is larger than the experimental results. This is expected, as there are many factors that contribute to achieve the theoretical SHG. To find how far off the experimental results are from the theory is simply determined by applying a coefficient to the theory, called the mode overlap. To find the best value for the mode overlap, the mean squared error between the fit and data is minimized. As discussed in Chapter 3 the cavity is not perfectly impedance matched, nor is it perfectly spatially mode matched. The losses in the cavity have also not been accurately measured, as this is a non trivial measurement to isolate scattering loss from the SHG loss. All of the extra losses and mode-overlap have been lumped together into the 74.0%, so the actual mode-overlap is better than this. In practice, the best coupling constant expected would be $\sim 90\%$. For the LBO the mode overlap is found to be 74.0% with a cavity loss of $\sim 0.5\%$. The theory with the applied mode overlap compared with the data is in Fig. 4.6b.

The low mode overlap here could be due to the mentioned factors. Based on more recent calculations, the spatial mode is probably contributing significantly to this mis-match and has been improved with better placements of the mode matching lenses and coupling into the cavity.

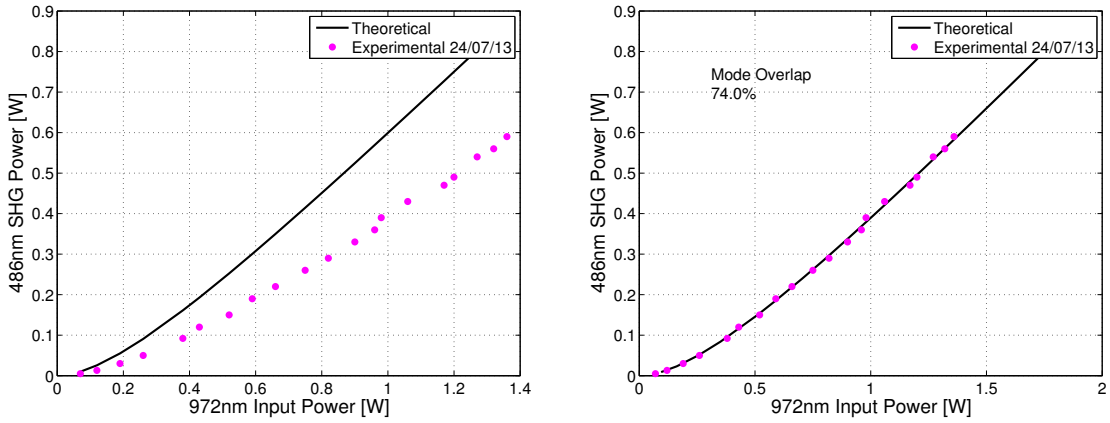

(a) Without mode overlap **(b)** With mode overlap

Figure 4.6: Experimental results of the nonlinear power conversion from 972 nm to 486 nm through the LBO crystal compared with the KNB theory. **(a)** Direct theory to experimental and **(b)** applying a mode overlap factor of 74.0% to the theory to match the experimental data.

BBO

Similar to the LBO cavity, Fig. 4.7 shows the theoretical results to the experimental data before and after the mode overlap is applied. Here the loss in taken to be 0.3% and the mode overlap is found to be 83.6%. This result is as expected and so it can be concluded the spatial mode matching and impedance matching are sufficient.

From the plots for both the LBO and BBO it is clear to see the conversion to the SHG are good.

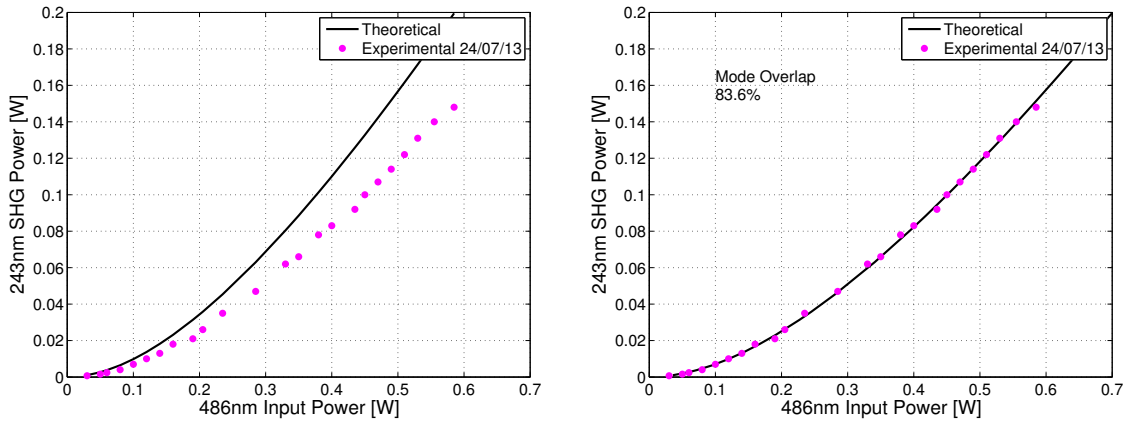

(a) Without mode overlap **(b)** With mode overlap

Figure 4.7: Experimental results of the nonlinear power conversion from 486 nm to 243 nm through the BBO crystal compared with KNB theory. **(a)** Direct theory to experimental and **(b)** applying a mode overlap factor of 83.6% to the theory to match the experimental data.

At the maximum input power of 1.4 W of 972 nm, the first stage produces 0.6 W of 486 nm, for an efficiency of 43%, and then second stage produces 150 mW of 243 nm light, for a 25% efficiency. This gives an overall efficiency of 11% from the IR to UV. For comparison, if a single pass method was used at both stages the overall efficiency would $\sim 0.01\%$. From these results it can be seen that enhancement cavities around the nonlinear crystals is the more effective method for producing UV light as relatively high powers.

Chapter 5

Measurement of the OPSL Linewidth

Accurately measuring the linewidth of a CW laser is non-trivial and narrowing the linewidth is even more of a challenge. Section 5.1 will present the purpose of measuring the linewidth and why it is experimentally important to narrow it. In Section 5.2 the new experimental setup will be discussed to highlight the various components that are required to make the measurement, like the Fabry-Perot stabilization cavity. Finally, Section 5.3 is where the theory and experimental results are presented for the linewidth measurement. Specifically, 5.3.1 will discuss the process of using a heterodyne beat signal to measure the frequency noise of a laser and 5.3.3 will develop the mathematical methods used to determine the linewidth from the frequency noise. Section 5.3.4 will conclude the results of the linewidth measurement, as well as look at methods to narrow the linewidth even farther. Finally, Section 5.3.5 will approximate how the linewidth from the 972 nm laser can be propagated through the SHG process to determine the linewidth at 243 nm.

5.1 Introduction and Motivation

An ideal monochromatic laser source would emit photons at a single frequency. This would look like a delta function on a frequency vs. amplitude plot, like the one in Fig. 5.1a. In reality the laser will have a minimum linewidth due to quantum noise fluctuations from spontaneous emission from the atoms in the laser cavity. This minimum limit in the linewidth, $\Delta\nu_{laser}$, is given by the Schawlow-Townes formula,

$$\Delta\nu_{laser} = \frac{4\pi h\nu\Delta\nu^2}{P_{out}}, \tag{5.1}$$

where $\Delta\nu$ is the resonator linewidth, $h\nu$ is the photon energy, and P_{osc} is the power of the laser [29]. Additionally, there are contributions to the laser linewidth that are due to mechanical vibrations, which usually out weigh the quantum noise. These linewidth contributions create a broader, Gaussian line shape centred at the laser frequency, shown in Fig. 5.1b. The width, FWHM, of this peak is known as the linewdith. Another way to think about linewidth, is how much time the laser is spending at a particular frequency, or wavelength. The more narrow the linewidth, the more time the laser is spending at the central frequency. Whereas with a larger linewidth the laser frequency

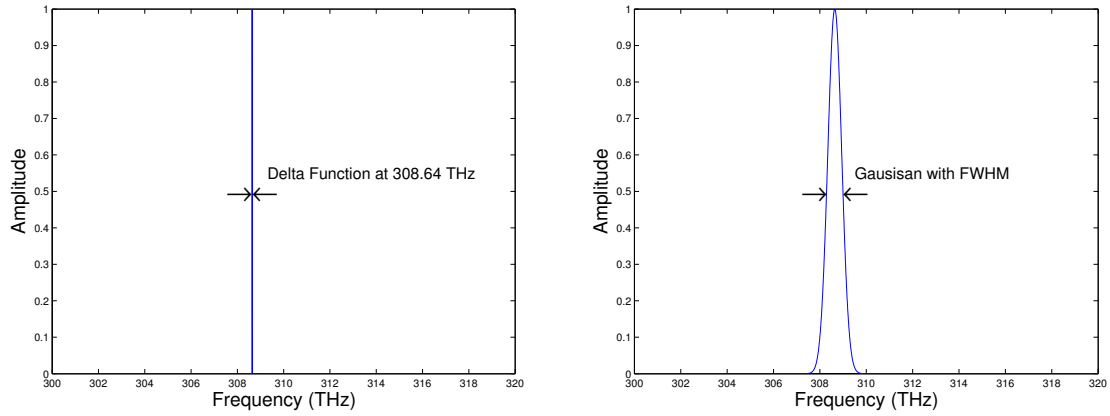

Figure 5.1: Schematic of laser linewidth at 308.64 THz, for an ideal delta function and a real Gaussian with some width, FWHM. **(a)** An ideal monochromatic laser with linewidth of zero, appearing as a delta function, and **(b)** a real laser with a Gaussian line shape and linewidth given by the FWHM [Note: scale is not representative of a real linewidth measurement]

is changing over a larger range and spends less time at the central frequency. Laser linewidths vary over a large range, from 1Hz to $>$ 10 GHz. There are many factors the contribute the the large and small linewidths. A free running laser will have a larger linewidth in the GHz range, where a stabilized diode laser can have a linewidth down in the Hz range. A HeNe laser can have a linewidth of about 10 kHz [15].

The natural, or free funning, linewidth of a diode laser is $\sim$1MHz, but can be narrowed down to $\sim$1Hz [21]. Similarly, with the OPSL used in this experiment, the linewidth can be narrowed from the MHz range to $<$1KHz. Narrowing the linewidth of a laser is as simple as locking it to a stabilization or Fabry-Perot cavity. Typically, to measure the linewidth, two lasers are locked to independent references and compared to one another. In this experiment the two lasers are locked together, in order to use the heterodyne beat to measure the relative linewidth. Both of these topics are further discussed in Sections 5.2.1 and 5.3.1, respectively, and the actual linewidth measurements of the OPSL are explained in detail in Section 5.3.

The above statements clearly state that it is possible to narrow the linewidth of a laser, but why is it important? Mentioned in the initial motivation for the development of the laser system in Section 1.1, this laser source is scheduled to be used in precision spectroscopy experiments. There are two reasons to have a narrow linewidth laser source for precision spectroscopy. Either simply to excite the atoms to a higher energy or to determine the exact energy required to make an energy transition. As described in Section 1.1.2, the use of the UV laser is to excite the ^{129}Xe atoms from the ground state with spin -1/2 and hyperfine level F = 1/2, to the 6p, spin 3/2 and F = 3/2. The linewidth simply needs to be less than 2 GHz, so as to not excite another energy transition. The first option for a laser source for the ^{129}Xe atoms has a linewidth larger than 2 GHz, so cannot be used

unless the linewidth is narrowed. Luckily, the OPSL has a free running linewidth in the MHz range, so satisfies this condition without any narrowing. This is not the case for all lasers, and so narrowing would need to be done.

Precision spectroscopy of Hydrogen is actually similar to the Xenon energy transition in that the atoms are excited from one state to another, however the goal is very different. In this case the goal is to determine the exact energy required for the atom to make this transition. Currently, this $1s$ to $2s$ is known to within an uncertainty of 10^{-15} as published by the H*ä*nsch group in 2013 [21]. One method for decreasing the uncertainty even further is to decrease the linewidth of the laser that is probing the transition. Since the transition is a two photon transition a narrower linewidth will greatly reduce the uncertainty on the measurement. For this reason, narrowing the linewidth of the OPSL is desired as this measurement is a future application of this laser. More about the Hydrogen measurements can be found in Section 1.1.1.

Now that the motivation has been established for measuring the linewidth of the laser and possibly narrowing it down if needed for future applications. It is not possible to simply propagate the light onto a photodetector and view the output on a spectrum analyzer and take the determine the linewidth. This is because the frequency of the light is on the order of hundreds of THz and fast electronics and a good spectrum analyzer only measure up to 30 GHz. Instead, what is done is called using a *heterodyne beat*, where two lasers with nearly the same frequency are overlapped onto a photodetector. The fields add such that the frequency measured is the difference between the two lasers. This difference can be tuned down to $<$1GHz so the relative linewidth can be evaluated. A more complete description and mathematical formulation of the heterodyne beat can be found in Section 5.3.1. The frequency noise is measured on a SRS network signal analyzer and then the relative linewidth between the two laser is deduced from this plot. The methods for determining the relative linewidth are detailed in Section 5.3.

Measuring the linewidth is the most important step, but the linewidth also needs to be narrowed for experiments like the Hydrogen spectroscopy. Typically lasers linewidths are narrowed by locking the laser to a stabilization cavity. This cavity is also known as a reference cavity, or Fabry-Perot cavity. Essentially, the stabilization cavity is fixed and the laser wavelength is locked to the length of the cavity. A more complete description of the Fabry-Perot cavity is detailed in Section 5.2.1. By locking the laser to this cavity, the frequency cannot drift freely with air circulation and temperature fluctuations, without the PZT in the laser changing oppositely to keep the frequency constant. The next section will outline the experimental setup for the linewidth measurement, followed by the various components used to narrow the linewidth and perform measurements.

5.2 Experimental Setup

This section will outline the new experimental setup that was used to measure the linewidth of the infrared OPSL. Fig. 5.2 shows a schematic of the setup. The main components present are the two OPSL lasers, labeled as the master and slave laser, the stabilization cavity and the mixing of the

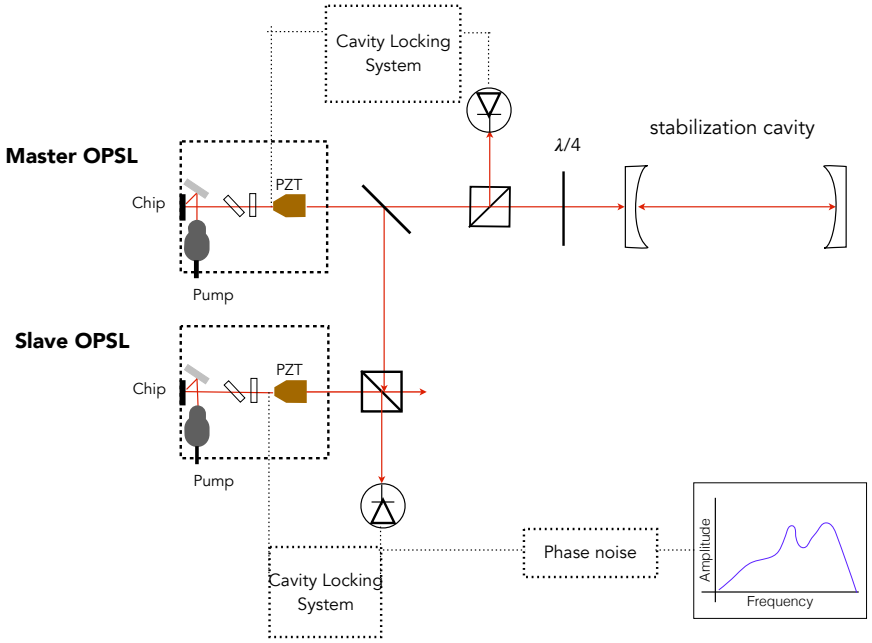

Figure 5.2: Schematic of the experimental set-up to measure the linewidth of the OPSL. There are two OPSL, one is the master laser that is locked to the Fabry-Perot stabilization cavity using a PDH locking scheme. The second is the slave laser that is locked to the beat between the two laser. This phase noise is derived from the lock at used to determine the linewidth of the slave laser.

lasers for the heterodyne beat used to measure the linewidth. There are also two locking systems indicated. The first is to lock the master laser to the stabilization cavity, and the second to lock the slave laser to the master laser.

There are several reasons for using two OPSL lasers. The first one was briefly mentioned in Section 5.1 to create a heterodyne beat, so the signal has a frequency that is detectable within the bandwidth of the electronics. It is required that both the lasers are of the same wavelength, as to get a small difference frequency in the beat signal. It would also be possible to split the beam from one laser and recombine it with an added frequency shift, however the two beams need to be uncorrelated, or decoupled from each other. This means that two lasers are required so that their noise is independent from one another. If the two lasers were correlated then the sum of the two fields would add and give a delta function.

It is also possible to do a self-heterodyne beat. To do this, the laser would first have to be split. One of the beam paths would require a delay, on a time scale longer than the coherence length, relative to the other beam. This will allow the beams to be uncorrelated and thus when the beams are mixed, the linewidths are added independently to make a larger linewidth. In both the dual laser and self-heterodyne beat cases, the measured linewidth is a relative linewidth between two

uncorrelated beams, and therefore larger than the linewidth of one laser. This larger linewidth is later accounted for in the linewidth calculation in Section 5.3.3. In Fig. 5.2 the heterodyne beat is shown at the bottom. This beat signal is also used to lock the slave laser to the master laser. This process is described in more detail in Section 5.3.1.

The next feature is the presence of the stabilization cavity. As mentioned in Section 5.1, the stabilization cavity is used to stabilize the master laser so that the servo that locks the slave to the master laser locks more effectively. If a laser is not controlled by any voltage on the PZT, the laser will naturally drift around and have a larger linewidth, or free running linewidth. Locking the slave laser to the master laser would force the servo to work much harder to maintain the lock, which could make the final linewidth measurement inaccurate. By locking the master laser to the Fabry-Perot cavity, the final relative linewidth measurement between the two lasers will be a more accurate measurement.

5.2.1 Fabry-Perot Stabilization Cavity

The stabilization cavity is a simple two mirror cavity, consisting of two curved mirrors with the same radius of curvature, radius of curvature (ROC). This geometry is also known as a Fabry-Perot cavity and was developed in the last two years of the 19th century by Charles Fabry and Alfred Perot [33]. The purpose of this cavity is very different compared to the two ring cavities used for the SHG. This cavity is purely used to stabilize the laser. The two SHG cavities have PZT's attached to one of the flat mirrors. Those cavities were then locked to the laser. As the laser freely drifts, the cavity PZT's adjust to change length to remain on resonance with the laser frequency. Here the opposite is true. The Fabry-Perot cavity is set to a fixed length by glueing the mirrors to a tube that minimizes changes in cavity length due to temperature fluctuations. The OPSL has a PZT attached to the output coupler mirror, which can be used to finely tune the wavelength of the laser to match the length of the cavity. Similar to the locking methods used for the SHG cavities, a PDH locking scheme is used here. The cavity is aligned and spatially mode matched so that the resonant transverse mode is the TEM_{00}. Once again the reflection signal off the input coupler is used to lock the laser frequency to the resonant peak.

Another difference between the SHG cavities and Fabry-Perot cavity is the resonant peaks of Fabry-Perot cavity are very narrow relative to the FSR, implying the cavity has a high finesse. It is ideal to have a very high finesse cavity for the stabilization cavity, because that means the linewidth is narrow. Recall the discussion of linewidth from Section 3.1.1, where the FWHM is the metric used as the linewidth of the signal. The linewidth is also directly comparable to the stability the cavity can provide for the laser. If the linewidth is narrow, the PDH lock will keep the laser to within a narrow range as large at the linewidth. The laser will not be able to drift around beyond the lock to the Fabry-Perot resonance. In the end, this reduces extra noise on the laser linewidth measurement that comes purely from drifting, rather than the actual linewidth of the laser.

To determine the finesse of the Fabry-Perot cavity a different method is used than the one from

Section 3.1.1. Here, finesse is determined by the reflectivity's of the mirrors by,

$$\mathcal{F} = \frac{\pi\sqrt{r_1 r_2}}{1 - r_1 r_2}, \tag{5.2}$$

where r_1 is the field reflectivity of the input coupler and r_2 is the reflectivity of the second mirror [22]. By definition, $r_1^2 + t_1^2 = 1$. The measured values for the reflectivity's are found to be, $r_1 = 0.99936$ and $r_2 = 0.99975$. Using the reflectivity's of the mirrors in Eq. 5.2, the finesse is found to be $\mathcal{F} = 7058$. This is considered a high finesse cavity and will provide significant stability to the master laser.

Once the master laser is locked to the Fabry-Perot stabilization cavity, the two lasers are beat together and the slave laser is locked to the master laser. The frequency noise from the slave laser is then measured to determine the linewidth.

5.3 Measuring the Linewidth

The linewidth of the laser is determined by measuring the frequency noise from the Fourier transform of the RF beat signal. This measurement involves the discussion of several kinds of frequencies. First is the frequency of the laser itself, or known as the optical frequency and denoted as ν. There will be two optical frequencies, once for each laser source and denoted as ν_0 and ν_1. When these two frequencies are beat together, as further described in the next section, the difference between their frequencies is given as, $\nu_1 - \nu_0 = f_c$, where f_c is the in RF region. It is also useful to write the carrier beat frequency, f_c as an angular frequency, ω_c, where $\omega_c = 2\pi f_c$. Finally, any additional frequency modulations on the carrier beat frequency will be denoted as Ω_m. The modulation frequencies will have some size corresponding to small deviations away from the carrier beat frequency, called frequency excursion and will be denoted by $\Delta\Omega$.

The next sections will discuss the heterodyne beat frequency, f_0, between the two laser sources. Then, this beat frequency is locked to a specific f_0 value. Then this signal is Fourier transformed to measurable modulation frequencies, Ω_m, with some frequency noise amplitude. From this frequency noise the relative linewidth between the two lasers can be determined and thus the linewidth of the laser.

5.3.1 Heterodyne Beat

It is first important to mathematically show how the heterodyne beat gives the difference between the two frequencies of the lasers interacting. The derivation of the intensity due to electric field of a wave is reproduced from Saleh and Teich [28]. First, it is important to start with one simple monochromatic wave, with an electric field given by,

$$E(t) = E_0 e^{-i(2\pi\nu_0)t - i\phi_0}, \tag{5.3}$$

where E_0 is the amplitude, ϕ_0 is the phase, and ν_0 is the optical frequency. For simplification, the phase can be set to zero, $\phi_0 = 0$, giving

$$E(t) = E_0 e^{-i(2\pi\nu_0)t}. \tag{5.4}$$

The frequency used in this experiment is 3.08×10^{13} Hz (or 972 nm). There are not electronics that have a bandwidth large enough to detect frequencies this high. If two waves with different frequencies, ν_0 and ν_1 are added together and written in terms of intensity, I, where

$$I = |E|^2 = |E_0 + E_1|^2, \tag{5.5}$$

then,

$$I = E_0^2 + E_1^2 + 2E_0E_1\cos[2\pi(\nu_1 - \nu_0)t]. \tag{5.6}$$

The term $(\nu_1 - \nu_0)$ is called the *heterodyne beat* frequency, and denoted as $\Delta\nu$ or f. If the two frequencies are close together and less than the bandwidth of the electronics, meaning < 1 GHz, then a signal can be detected. This is exactly what is done in the lab. The two lasers are overlapped and focused onto a photodiode detector. The intensity in the beams are adjusted so $I_1 = I_2$, thus reducing Eq. 5.6 to,

$$I = 2I_0\big[1 + \cos[2\pi(\nu_1 - \nu_0)t]\big]. \tag{5.7}$$

5.3.2 Locking the Slave Laser to the Master Laser

The frequency noise comes directly from this heterodyne beat. Before diving into the full evaluation of the frequency noise and linewidth measure, the methods for narrowing the linewidth must be established. The master laser is locked to the stabilization cavity using the PDH method as outlined in Section 3.3. This time the laser is locked to the cavity in order to take out the long term drift of the master laser. Since the optical frequency of this laser can be measured the slave laser is beat with the master laser to make and RF frequency. The slave laser is still free running, so the heterodyne beat is a combination of the stable master laser and the free running slave laser. A linewidth measurement of this beat, would result in a broad linewidth, mostly composed of the drifting of the slave laser. To minimize this, the slave laser can be locked to the master laser.

The heterodyne beat frequency can be manually adjusted by simply tuning the wavelength of the slave laser. If the frequency of an external synthesizer is set close to the frequency of the beat, then the slave laser can be locked such that the beat frequency remains the same as the external, or reference frequency. The PZT attached to the output coupler in the laser cavity controls the length of the laser cavity in order to maintain the beat frequency. The frequency of the master laser is only varying within the linewidth of the stabilization cavity. Thus, by locking the slave laser to the beat frequency the linewidth of the slave laser linewidth is reduced. From here, the relative linewidth of the beat frequency can be determined. Assuming the two lasers are uncorrelated the linewidth of one laser can be approximated as linewidth of the beat divided by $\sqrt{2}$.

5.3.3 Frequency Noise and the β-line

Once the linewidth of the slave laser has been reduced, the RF signal from the heterodyne beat can be converted into frequency noise. It was established that the heterodyne beat produces a wave with a frequency given by the difference between the two optical frequencies, $\nu_1 - \nu_0$. This difference is decreased until it lies within the RF region and detectable by common electronics, this new frequency will is denoted as f_c and the angular frequency ω_c, where $\omega_c = 2\pi f_c$.

The derivation of frequency noise starts with frequency modulation theory described by John Hall and Miao Shu [15]. A simple monochromatic beam with phase-modulation, $\phi(t)$, is written as an electric field by,

$$E(t) = E_0 e^{-i\omega_c t - i\phi(t)}. \tag{5.8}$$

Since the field exhibits a phase modulation in real life, this can be represented by

$$\phi(t) = \beta \sin \Omega_m t, \tag{5.9}$$

where Ω_m is the modulation frequency and β is the modulation index. The argument of *phase modulation* on the centre frequency can also be written in terms of *frequency modulation*. The relationship between frequency and phase is, $\omega = d\phi(t)/dt$. If the instantaneous frequency is defined as $\omega(t)$, then,

$$\omega(t) = \omega_c + \frac{d}{dt}\phi(t) \tag{5.10}$$

$$\omega(t) = \omega_c + \beta\Omega_m \cos \Omega_m t. \tag{5.11}$$

This relationship shows the significance of β, either in the case of phase or frequency modulation. Another way to define β is as the frequency excursion divided by the frequency modulation rate, $\beta = \Delta f / f_m$. The excursion frequency is a measure of how far away the frequency is from the carrier frequency and denoted as Δf, where $\Delta f = f - f_c$ and $\omega = 2\pi f$ and $\omega_c = 2\pi f_c$. The modulation frequency of the excursion frequency is denoted as f_m, where $\Omega_m = 2\pi f_m$.

The RF signal from the heterodyne beat is sent into an SRS network signal analyzer, where the signal is Fourier transformed into the various modulation frequency components. To describe how this signal appears on the SRS network signal analyzer, as shown in Fig. 5.5, it is important to have an understanding of frequency modulation theory and the conceptual idea of β. For a small Δf, meaning a small frequency distance from the carrier frequency, and a fast modulation rate, f_m, than $\beta \ll 1$. The contribution from this type of noise to the linewidth will be very small. Then for large Δf and slow f_m, $\beta > 1$, meaning the modulation index is high and this noise contributes significantly to the linewidth.

The frequency variation per unit bandwidth at a frequency Δf from the carrier frequency of the heterodyne beat signal gives the frequency noise spectral density, denoted by, $S_{\delta f}(f_m)$, over the

modulation frequencies. The spectral density is given by,

$$S_{\delta f}(f_m) = \frac{\Delta f_{rms}(f_m)^2}{b} \quad \left[\frac{Hz^2}{Hz}\right], \tag{5.12}$$

where b is the bandwidth, or bin size of the modulation frequency, $\Delta f_{rms}(f_m)$ is frequency excursion from the beat carrier frequency, f_c, and f_m is the Fourier modulation frequency [15].

There are several methods presented throughout the literature for evaluating the frequency noise to determine the linewidth of a laser. John Hall and Miao Zhu [15] give a comprehensive explanation of phase and frequency noise for optical sources. As well as one method for determining the linewidth of the source, based on the spectral density of the phase and frequency noise. A more refined evaluation of the spectral density and how the frequency noise contributes to the linewidth of the optical source is described by Domenico, Schilt and Thomann (DST) [9]. This second method is the one chosen to determine the linewidth of the OPSL in this experiment. The DST approach considers how the frequency excursions depend on the range of modulation frequencies and thus contribute to the linewidth.

An outline of the DST work will be described here to highlight the key components that are used to determine the linewidth of the laser. A complete and mathematical description of their study and results can be found in the DST paper, [9]. As mentioned, various frequency components contribute differently to the linewidth of the source, for example a low modulation frequency with a large excursion from the carrier beat frequency will increase the linewidth of the source. Whereas, fast modulations at low excursion frequencies do not contribute to the linewidth, but do contribute to the line shape. DST establishes a function that separates the significant linewidth contributions from the insignificant ones, by means of the point when the line shape changes. This function is known as the β-separation line.

To establish the β-separation line, a conceptual description of the transition in the line shape is illustrated in Fig. 5.3a. The line shape is broken down into different regions, from a to d. In regions a and b the line shape is Gaussian and remains Gaussian, but with an expanding linewidth. Beginning in region c and more clearly in region d, the line shape is Lorentzian and the linewidth is no longer changing. This transition from a Gaussian line shape to a Lorentzian line shape is the point which corresponds to the ratio between the modulation frequency, f_m, and the frequency noise level, called h_o [Hz^2/Hz] for now. DST use a simple model to describe this point where the line shape changes. They start with a constant frequency noise, h_o, that depends on f_m as a step function. So at a given frequency, called the cut-off frequency, f_{cut}, the frequency noise level changes from h_o to zero. For a fixed value of h_o and as the cut-off frequency increases from zero, there is a f_{cut} which corresponds to the point when line shape changes from a Gaussian to a Lorentzian. Mathematically this can be modelled as a autocorrelation function, as described in the work of DST [9].

To maintain the focus on the conceptual understanding, it is safe to jump ahead to the FWHM representation of the spectral noise density. DST describes the mathematical approach to finding a

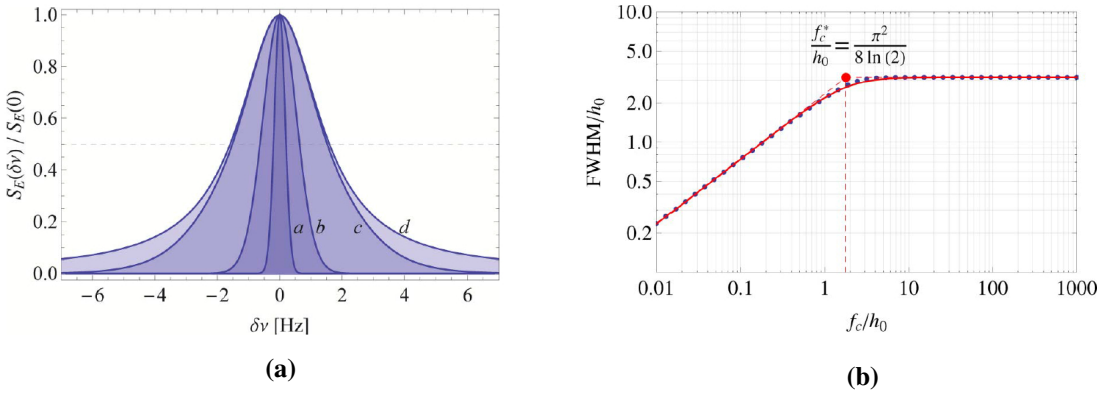

Figure 5.3: Evolution of Gaussian line shape to a Lorentzian line shape. **(a)** Shows the evolution from a Gaussian line shape to a Lorentzian line shape from regions a to d, where the x-axis is the linewidth and the y-axis is relative amplitude [9]. **(b)** Shows the evolution of the linewidth for an increasing frequency to noise level ratio, f_{cut}/h_o. The indicated point where the linewidth stops growing corresponds to the transition from the Gaussian to the Lorentzian line shape [9].

clean result of the FWHM for a changing f_{cut}. This is given by,

$$FWHM = h_o \frac{\sqrt{8ln(2)f_{cut}/h_o}}{\left[1 + \left(\frac{8ln(2)f_{cut}}{\pi^2 h_o}\right)^2\right]^{1/4}}. \tag{5.13}$$

The visual representation is even more useful and shown in Fig. 5.3b. This plot shows how the FWHM evolves for a growing f_{cut} relative to the noise level, h_o. At a cutoff frequency to noise ratio, the linewidth increases linearly, until a point and then the linewidth remains constant. This point occurs at, $f_{cut}/h_o = \pi^2/8ln(2)$. This transition is directly related to the transition from a Gaussian line shape to the Lorentzian line shape.

The ideas presented about how the relationship between the noise level, h_0, and the cut-off frequency contribute to the linewidth can be directly applied to the frequency noise from a laser. High index frequency modulations contribute directly to the Gaussian line shape and therefore to the linewidth. Whereas, fast modulations with low index modulations do not effect the linewidth and only contribute to the Lorentzian line shape. This metric is the β-separation line. Fig. 5.4 shows a schematic of the β-separation line and the various modulation index levels [9]. When $S_{\delta f}(f_m) > 8ln(2)f_m/\pi^2$ the modulations have a high index and therefore contribute to the Gaussian lineshape and thus the linewidth. Whereas, when $S_{\delta f}(f_m) < 8ln(2)f_m/\pi^2$, the modulation index is lower therefore only contributes to the wings of the line shape and not the linewidth.

Now, that the conceptual understanding of the β-separation line has been established. The mathematical determination of the linewidth can now be implemented. The linewidth of the laser

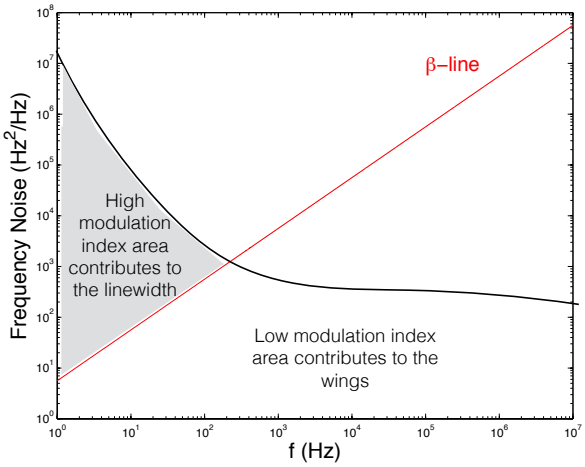

Figure 5.4: Illustration the β-separation line for an arbitrary frequency noise spectrum. Indicated are the regions where the high modulation at low frequencies contribute to the linewidth and low modulations at high frequencies lie below the β-separation line as they do not contribute to the linewidth.

source can be described as the FWHM, where

$$FWHM = \frac{\sqrt{8ln(2)A}}{\sqrt{2}}. \tag{5.14}$$

The variable A is the integration under the frequency noise curve above the β-separation line as shown shaded in grey in Fig. 5.4. The $\sqrt{2}$ is used to account for the two lasers being uncorrelated with each other. Since the signal used to measure the linewidth is the beat between the master and slave laser, the linewidth is a combination of the two separate linewidths. This produces a slightly larger linewidth and therefore needs to be reduced by the factor of $\sqrt{2}$ to approximate the linewidth from just the slave laser. The integration variable, A, can be expressed as follows,

$$A = \int_{1/T_o}^{\infty} H(S_{\delta f}(f_m) - 8ln(2)f_m/\pi^2)S_{\delta f}(f_m)df, \tag{5.15}$$

where H(x) is the Heaviside function, and the integration is over the frequency from $1/T_o$ to ∞. T_o is the measurement period limit. This means that frequencies lower than $1/T_o$ cannot be measured. The T_o in this linewidth measurement is $T_o = 1$ s, or $1/T_o = 1$ Hz. When $x \leq 0$, meaning the frequency noise is below the β-line, then $H(x) = 0$, and when $x > 0$ and the frequency noise is greater than the β-line, $H(x) = 1$. When $H(x) = 1$, then Eq. 5.15 simplifies to a simple integral,

$$A = \int_{1/T_o}^{\infty} S_{\delta f}(f_m)df, \tag{5.16}$$

for specific f_m values.

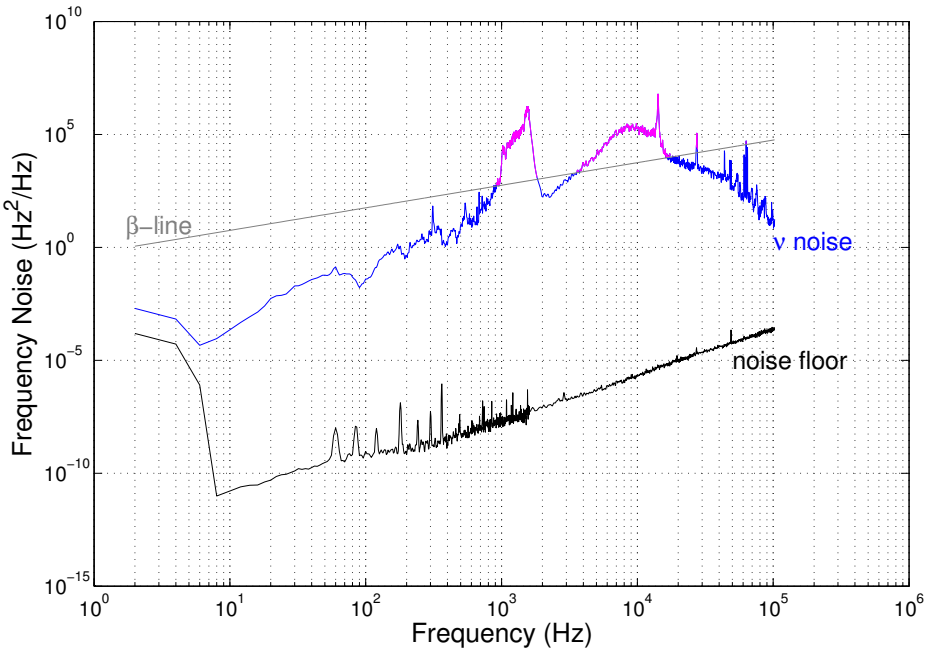

Figure 5.5: Measuring the linewidth from frequency noise plot. The frequency noise between two lasers beat together, while one laser is stabilized to a Fabry-Perot cavity, is shown in blue. This data has been reduced by subtracting off the data in black, which is the background noise from the electronics. The frequencies with a high enough amplitude in frequency space, denoted as frequency noise, above the labeled β-line gives the linewidth of the laser, at 87 kHz.

On a frequency noise plots, integrating over the frequencies with frequency noise above the β-line will give the linewidth of the laser. The results of the linewidth measurement from the OPSL laser are presented in the next section.

5.3.4 Results and Discussion

The results of the frequency noise from the OPSL, when the slave laser is locked to the master laser and the master laser is locked to the stabilization cavity are presented in Fig. 5.5. It is important to note that there is a noise floor present in the plot. This was measured by blocking the optical signal on the photodiode and simply measuring the static noise from the electronics. When the phase noise was analyzed, the noise floor was subtracted off to minimize false additions to the linewidth measurement.

The β-separation line is also displayed in Fig. 5.5. Above the line, the signal is outlined in pink to show the part of the frequency noise that contributes to the linewidth. Solving Eq. 5.14, the result gives a linewidth of **87 KHz**.

The OPSL has the potential to have a narrow linewidth < 1 kHz. From the results of these initial

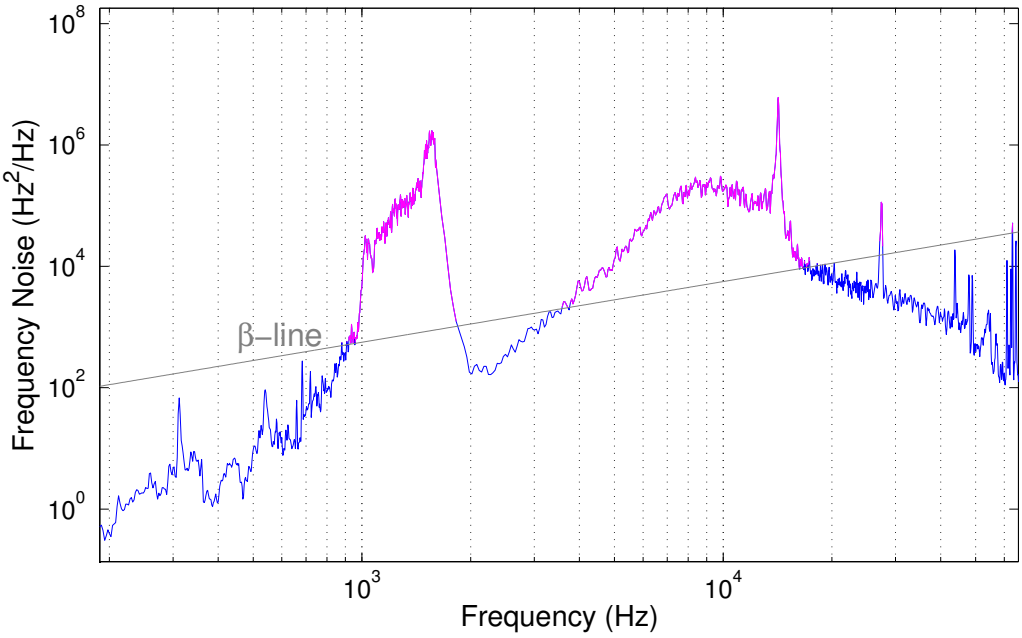

Figure 5.6: Close-up view of the frequencies mainly contributing to the laser linewidth. The hump on the left is known as the servo bump and then highest peak on the right hump, around 1.7 kHz comes from a mechanical resonance in the laser. The official source remains unknown. If both of those humps can be minimized, the linewidth of the laser will narrow.

measurements, the linewidth is 87 kHz. This is not as low as expected but, there many components that contribute to the narrowing of this linewidth and all need to be optimized for the best linewidth measurement. The lock of the master laser to the stabilization cavity may be a weak lock, so the linewidth is not narrowed as far as it could be. The lock of the slave laser to the master laser could also be a tighter lock, decreasing the added fluctuations to the linewidth. To help with some of these variables, a box was placed around the stabilization cavity and the master laser to reduce vibrations from noise. The lasers were placed on separate bread boards to help maintain uncorrelated vibrations and also decrease vibrations that occur on the main optical table. It was with these adjustments that the linewidth was narrowed down to the 87 KHz, from the first measurements of a few hundred KHz. More improvements could be made to continue optimizing the locks and minimizing environmental vibrations.

There are also several features to mention on the frequency noise plot in Fig. 5.5 that have large contributions to the linewidth. The first is the servo bump, which is the bump at the higher frequencies in Fig. 5.6. This bump represents the frequency noise from the electronic components used to lock the lasers and measure the noise. It is possibly to minimize this bump, but there will always be a servo bump present. Changing the impedence values on some of the locking components was able to decrease the servo bump to what is shown in Fig. 5.6.

The other feature to note is the peak around 1.7 kHz in Fig. 5.6. This peak is not from either the electrical noise or from the linewidth, but rather is a peak associated with a mechanical resonance or technical noise. This peak has been observed in other OPSL lasers, so can be concluded that it is not an environmental resonance. It is possible this resonance is amplitude noise of the OPSL pump, but this is yet to be confirmed. However, it can be concluded this 1.7 KHz is not truly part of the laser linewidth and once the source of the noise is located and suppressed, the linewidth of the laser will reduce.

Overall, the measurement of 87 kHz is a good first measurement. But, if the 1.7 kHz bump can be minimized or eliminated than the linewidth can be narrowed even farther, pushing < 1 kHz at 972 nm.

5.3.5 Approximation of the Linewidth at 243 nm

The linewidth of the 972 nm was measured, but an approximation can be made for how this linewidth would translate through the SHG and to the 243 nm light. Through the analysis of the linewidth, the β-separation line limits the line shape to be a Gaussian given by,

$$L(\nu) = Ae^{-\frac{(\nu-\nu_0)^2}{2\sigma_\nu^2}}, \tag{5.17}$$

where ν is the variable frequency, ν_0 is the central frequency, and σ_ν is the FWHM, or linewidth of the line shape. The SHG process means the frequency of the fundamental doubles, $\nu_2 = 2\nu$ and $\nu_{02} = 2\nu_0$, but how is σ_ν related to σ_{ν_2}?

Since the process is a two photon process, each photon has the probability of laying anywhere within the linewidth distribution. Therefore the linedwiths of the two photons are multiplied together, to account for any combination of energies that give the correct total energy required,

$$L_1(\nu)L_2(\nu) = Ae^{-\frac{(\nu-\nu_0)^2}{2\sigma_\nu^2}} * Ae^{-\frac{(\nu-\nu_0)^2}{2\sigma_\nu^2}} = A^2e^{-\frac{2(\nu-\nu_0)^2}{2\sigma_\nu^2}}. \tag{5.18}$$

The distribution for the second harmonic can be expressed as a Gaussian as well and equated to the two photon Gaussian,

$$L(\nu_2) = Be^{-\frac{(\nu_2-\nu_{02})^2}{2\sigma_{\nu_2}^2}} = A^2e^{-\frac{2(\nu-\nu_0)^2}{2\sigma_\nu^2}}, \tag{5.19}$$

Where B = A^2. The exponents can be equated to find the relationship between the linewidths,

$$-\frac{(\nu_2-\nu_{02})^2}{2\sigma_{\nu_2}^2} = -\frac{2(\nu-\nu_0)^2}{2\sigma_\nu^2}. \tag{5.20}$$

Substituting in the relationship between the two frequencies, i.e. $\nu_2 = 2\nu$ and $\nu_{02} = 2\nu_0$, and can-

celling the two's on the right side of Eq. 5.20 gives,

$$\frac{(2\nu - 2\nu_0)^2}{2\sigma_{\nu_2}^2} = \frac{(\nu - \nu_0)^2}{\sigma_\nu^2}. \tag{5.21}$$

Simplifying,

$$\frac{4}{2\sigma_{\nu_2}^2} = \frac{1}{\sigma_\nu^2}, \tag{5.22}$$

and

$$2\sigma_\nu^2 = \sigma_{\nu_2}^2, \tag{5.23}$$

thus,

$$\sqrt{2}\sigma_\nu = \sigma_{\nu_2}. \tag{5.24}$$

This approximation shows that the linewidth through second harmonic generation increases by $\sqrt{2}$ from the fundamental linewidth. The same approximation can be used for the second stage of second harmonic generation. Therefore,

$$\sigma_{\nu_4} = 2\sigma_\nu, \tag{5.25}$$

and the linewidth at 243 nm is $\sim$174 kHz for 87 kHz linewidth at 972 nm.

Another quantity to consider is the quality factor, Q, and spectral resolution. The quality factor is defined as,

$$Q = \frac{\nu}{\sigma_\nu}. \tag{5.26}$$

Comparing the fundamental to the 4th harmonic,

$$\frac{\nu_4}{\sigma_{4\nu}} \rightarrow \frac{4\nu}{2\sigma_\nu}, \tag{5.27}$$

therefore,

$$Q_{4\nu} = 2Q_\nu. \tag{5.28}$$

The inverse of the quality factor is the spectral resolution which is an important ratio for precision spectroscopy. In this case the spectral resolution of the 4th harmonic is half the resolution of the fundamental. A higher spectral resolution will decrease the uncertainty in the overall spectroscopy measurements. However, even though the laser frequency is quadrupled the spectral resolution only drops by half.

Chapter 6

Conclusion and Future Work

An IR OPSL was successfully used to generate UV light for the use in precision spectroscopy experiments. The IR light was frequency doubled twice to generate 150 mW of 243 nm light. The linewidth of the OPSL was also measured to be ~ 87 kHz.

The process to generate UV light started with 1.7 W of CW light from the OPSL at 972 nm. Two stages of enhancement cavities with nonlinear crystals were used in series with the laser to frequency double the light twice down to 243 nm. The enhancement cavities have a bow-tie geometry to allow the light to propagate in one direction through the cavity and also through the nonlinear crystal, generating a uni- directional beam of second harmonic light. The enhancement cavity allows for a more efficient SHG process, because the buildup of light inside the enhancement cavity is 60-90 times the intensity of the input light. If the single pass process was used, the combination of the two frequency doubling stages would result in an efficiency of $\sim 0.01\%$. By placing the nonlinear crystals inside enhancement cavities, an efficiency of 11% was achieved, with a total at 150 mW of 243 nm light. The first enhancement cavity used an LBO crystal and a BBO in the second enhancement cavity.

The second part of the experiment was to measure the linewidth of the OPSL. This was done by using two uncorrelated OPSLs. The first laser was stabilized to a Fabry-Perot cavity. The two lasers were beat together, to generate a measurable heterodyne beat. This signal was first used to lock the second laser to the first laser. Then the frequency noise of the beat signal was used to determine the relative linewidth between the two lasers. A careful analysis and separation of the frequency noise associated with the true relative linewidth, yielded a linewidth of one OPSL to be 87 kHz. The linewidth was successfully narrowed from the free running linewidth on the order of several hundred MHz. However, the linewidth is still dominated by frequency noise due to mechanical or technical vibrations and has the potential to be narrowed even further.

The narrow linewidth and high UV power of the OPSL and frequency doubling cavities have serious implications in the field of precision spectroscopy. This laser system is currently being replicated at the wavelength to drive a transition in ^{129}Xe from the ground state. The future of this laser system is part of the UCN collaboration to measure the EDM of the neutron. The first measure-

ment will establish the ^{129}Xe two photon transition labeled in Fig. 1.3b. Then, the EDM of ^{129}Xe needs to be measured with a higher precision than current measurements, which is $|d(^{129}Xe)| < 4.1$ x $10^{-27}e$ cm [25]. This will be performed using the same methods as described in Section 1.1.2. Finally, ^{129}Xe will be combined with ^{199}Hg as a dual co-magnetometer for the measurement of neutron EDM.

Bibliography

[1] A. Ashkin, G. D. Boyd, and J. M. Dziedzic. Observation of continuous optical harmonic generation with gas masers. *Phys. Rev. Lett.*, 11:14–17, Jul 1963. doi:10.1103/PhysRevLett.11.14. URL http://link.aps.org/doi/10.1103/PhysRevLett.11.14. → pages 12

[2] A. Ashkin, G. Boyd, and J. Dziedzic. Resonant optical second harmonic generation and mixing. *IEEE Journal of Quantum Electronics*, 2(6):109–124, 1966. → pages 12, 40

[3] C. Baker, Y. Chibane, M. Chouder, P. Geltenbort, K. Green, P. Harris, B. Heckel, P. Iaydjiev, S. Ivanov, I. Kilvington, et al. Apparatus for measurement of the electric dipole moment of the neutron using a cohabiting atomic-mercury magnetometer. *Nuclear Instruments and Methods in Physics Research Section A: Accelerators, Spectrometers, Detectors and Associated Equipment*, 736:184–203, 2014. → pages 3, 4

[4] A. Berry. *Henry Cavendish, his life and scientific work*. Hutchinson, 1960. → pages 1

[5] E. D. Black. An introduction to pound-drever-hall laser frequency stabilization. *American Journal of Physics*, 69(1):79–87, 2001. → pages 13, 25, 28, 29, 30, 31

[6] G. Boyd and D. Kleinman. Parametric interaction of focused gaussian light beams. *Journal of Applied Physics*, 39(8):3597–3639, 1968. → pages 39, 40

[7] R. Boyd. Nonlinear optics. 1992. → pages 34

[8] C. Chen, T. Sasaki, R. Li, Y. Wu, Z. Lin, Y. Mori, Z. Hu, J. Wang, G. Aka, M. Yoshimura, et al. *Nonlinear Optical Borate Crystals: Principals and Applications*. EngineeringPro collection. Wiley, 2012. ISBN 9783527646418. URL http://books.google.ca/books?id=uUB-Q-MFdJkC. → pages 7, 12, 40

[9] G. Domenico, S. Schilt, and P. Thomann. Simple approach to the relation between laser frequency noise and laser line shape. *Applied Optics*, 49(25):4801–4807, 2010. → pages 52, 53

[10] R. W. P. Drever, J. L. Hall, and F. V. Kowalski. Laser phase and frequency stabilization using an optical resonator. *Applied Physics B*, 31(31):97–105, 1983. → pages 26

[11] J. Ellis. Theory of the neutron electric dipole moment. *Nuclear Instruments and Methods in Physics Research Section A: Accelerators, Spectrometers, Detectors and Associated Equipment*, 284(1):33–39, 1989. → pages 2

[12] P. A. Franken, A. E. Hill, C. W. Peters, and G. Weinreich. Generation of optical harmonics. *Phys. Rev. Lett.*, 7:118–119, Aug 1961. doi:10.1103/PhysRevLett.7.118. URL http://link.aps.org/doi/10.1103/PhysRevLett.7.118. → pages 12

[13] J. A. Giordmaine. Mixing of light beams in crystals. *Phys. Rev. Lett.*, 8:19–20, Jan 1962. doi:10.1103/PhysRevLett.8.19. URL http://link.aps.org/doi/10.1103/PhysRevLett.8.19. → pages 12

[14] W. C. Griffith, M. D. Swallows, T. H. Loftus, M. V. Romalis, B. R. Heckel, and E. N. Fortson. Improved limit on the permanent electric dipole moment of ^{199}Hg. *Phys. Rev. Lett.*, 102: 101601, Mar 2009. doi:10.1103/PhysRevLett.102.101601. URL http://link.aps.org/doi/10.1103/PhysRevLett.102.101601. → pages 3

[15] J. L. Hall and M. Zhu. *An introduction to phase-stable optical sources*, volume CXVIII. North-Holland, 1993. JILA Pub. 4738. → pages 29, 45, 51, 52

[16] P. G. Harris, C. A. Baker, K. Green, P. Iaydjiev, S. Ivanov, D. J. R. May, J. M. Pendlebury, D. Shiers, K. F. Smith, M. van der Grinten, and P. Geltenbort. New experimental limit on the electric dipole moment of the neutron. *Phys. Rev. Lett.*, 82:904–907, Feb 1999. doi:10.1103/PhysRevLett.82.904. URL http://link.aps.org/doi/10.1103/PhysRevLett.82.904. → pages 2

[17] E. P. Ippen. 6.634 nonlinear optics. Lecture notes, 1996. Massachusetts Institute of Technology. → pages 37, 38

[18] Y. Kaneda. Research Professor at the University of Arizona, College of Optical Sciences,1630 E. University Blvd, P.O. Box 210094, Tucson, AZ 85721-0094. → pages 9, 10, 11

[19] W. Kozlovsky, C. Nabors, and R. Byer. Iefficient second harmonic generation of a diode-laser-pumped cw nd:yag laser using monolithic $mgo : linbo_3$ external resonant cavities. *IEEE Journal of Quantum Electronics*, 24(6):913–919, 1988. → pages 12, 40

[20] P. D. Maker, R. W. Terhune, M. Nisenoff, and C. M. Savage. Effects of dispersion and focusing on the production of optical harmonics. *Phys. Rev. Lett.*, 8:21–22, Jan 1962. doi:10.1103/PhysRevLett.8.21. URL http://link.aps.org/doi/10.1103/PhysRevLett.8.21. → pages 12

[21] A. Matveev, C. G. Parthey, K. Predehl, J. Alnis, A. Beyer, R. Holzwarth, T. Udem, T. Wilken, N. Kolachevsky, M. Abgrall, D. Rovera, C. Salomon, P. Laurent, G. Grosche, O. Terra, T. Legero, H. Schnatz, S. Weyers, B. Altschul, and T. W. Hänsch. Precision measurement of the hydrogen 1*s*-2*s* frequency via a 920-km fiber link. *Phys. Rev. Lett.*, 110:230801, Jun 2013. doi:10.1103/PhysRevLett.110.230801. URL http://link.aps.org/doi/10.1103/PhysRevLett.110.230801. → pages 1, 2, 45, 46

[22] W. Nagourney. *Quantum Electronics for Atomic Physics*. Oxford University Press, 2 edition, 2010. ISBN 9780199532629. → pages 17, 20, 25, 34, 35, 38, 39, 49

[23] R. V. Pound. Electronic frequency stabilization of microwave oscillators. *Review of Scientific Instruments*, 17(11):490–505, 1946. → pages 26

[24] N. F. Ramsey. Electric-dipole moments of elementary particles. *Reports on progress in physics*, 45(1):95, 1982. → pages 2

[25] M. A. Rosenberry and T. E. Chupp. Atomic electric dipole moment measurement using spin exchange pumped masers of ^{129}Xe and ^{3}He. *Phys. Rev. Lett.*, 86:22–25, Jan 2001. doi:10.1103/PhysRevLett.86.22. URL http://link.aps.org/doi/10.1103/PhysRevLett.86.22. → pages 60

[26] R. L. Sacramento, B. X. Alves, D. T. Almeida, W. Wolff, M. S. Li, and C. L. Cesar. Source of slow lithium atoms from ne or h2 matrix isolation sublimation. *Journal of Chemical Physics*, 136(15):154202, 2012. ISSN 00219606. URL http://search.ebscohost.com.ezproxy.library.ubc.ca/login.aspx?direct=true&db=a9h&AN=74464635&site=ehost-live&scope=site. → pages 2

[27] J. Sakurai and J. Napolitano. *Modern Quantum Mechanics*. ??????? Addison-Wesley, 2011. ISBN 9780805382914. URL http://books.google.ca/books?id=N4I-AQAACAAJ. → pages 4

[28] B. E. A. Saleh and M. C. Teich. *Fundamentals of Photonics*. John Wiley & Sons, INC.s, 2 edition, 2007. ISBN 9780471358329. → pages 20, 21, 22, 49

[29] A. L. Schawlow and C. H. Townes. Infrared and optical masers. *Phys. Rev.*, 112:1940–1949, Dec 1958. doi:10.1103/PhysRev.112.1940. URL http://link.aps.org/doi/10.1103/PhysRev.112.1940. → pages 44

[30] A. Siegman. *Lasers*. University Science Books, 1 edition, 1986. ISBN 0935702113. → pages 10, 11

[31] A. V. Smith. Snlo software codes. AS-Photonics. Albuquerque, NM. → pages 38

[32] J. H. Smith, E. M. Purcell, and N. F. Ramsey. Experimental limit to the electric dipole moment of the neutron. *Phys. Rev.*, 108:120–122, Oct 1957. doi:10.1103/PhysRev.108.120. URL http://link.aps.org/doi/10.1103/PhysRev.108.120. → pages 2

[33] M. Vaughan. *The Fabry-Perot interferometer: history, theory, practice and applications*. CRC press, 1989. → pages 48

[34] T.-L. Wang et al. High-power optically pumped semiconductor laser at 1040 nm. *IEEE Photonics Technology Letters*, 22(9):661–663, 2010. → pages 9, 10